Development of a Novel Fiber Laser Based Backward-Mode Photoacoustic Microscopy System and Image Characterization

by

Mustafa Ümit Arabul

B.S., Electrical and Electronics Engineering, Middle East Technical University, 2011

Submitted to the Institute of Biomedical Engineering
in partial fulfillment of the requirements
for the degree of
Master of Science
in
Biomedical Engineering

Boğaziçi University
2013

ACKNOWLEDGMENTS

To begin with, I would like to express my very great appreciation to my thesis advisor Prof. Cengizhan Öztürk for his precious guidance and support towards photoacoustic imaging.

I would like to express my deepest gratitude to my co-advisor Assoc. Prof. Dr. Mehmet Burçin Ünlü for his irreplaceable encouragement and valuable support beyond supervising through this dissertation. It would not be possible to achieve this project without his incontrovertible sustenance.

I would like to offer my special thanks to Assoc. Prof. Dr. F. Ömer İlday and Seydi Yavaş for their collaboration and endless support in laser design. My special thanks are extended to the all members of Ultrafast Optics Laboratory in Bilkent University.

I wish to acknowledge the valuable efforts and assistance provided by my colleagues in photoacoustic microscopy project, Hakan Erkol and Esra Aytaç - Kipergil. Their perspective as physicists invaluably became supportive and inspiring for me, and I am grateful for being part of such an interdisciplinary research group. I would like to thank for their friendship beyond a colleagueship.

Regrettably, I cannot acknowledge them by name, yet I am grateful to all the colleagues in the Institute of Biomedical Engineering, who supported me with their inspiring advices.

I would also like to thank my family for being there and supporting me through my research career.

Finally, with all sincerity of my heart, I would like to thank my prospective wife Demet Altun for her support, encouragement and love.

ABSTRACT

Development of a Novel Fiber Laser Based Backward-Mode Photoacoustic Microscopy System and Image Characterization

Among all other imaging modalities, optical methods using non-ionizing radiation became popular due to safety concerns. However, pure optical methods have severe limitations for deep tissue imaging. On the other hand, photoacoustic imaging is a promising imaging modality for *in vivo* tissue monitoring due to its high optical contrast and high ultrasonic resolution. The parameters of the laser used in photoacoustics, namely pulse duration, pulse repetition frequency, beamwidth and output power has a quantifiable impact on signal amplitude, imaging speed and resolution. In literature, Q-switched lasers, solid state lasers and fiber lasers are used for the microscopic scale of photoacoustic imaging. Most of the lasers used in photoacoustic studies has a fixed capacity and key parameters cannot be adjusted independently. In this study, we declare a novel all-fiber mode-locked laser with adjustable pulse duration between 1 - 3 ns and selectable pulse repetition frequency between 50 kHz and 3.1 MHz. All fiber integration makes our laser resistant to vibrational disturbances, yet increases its stability. Additionally, we utilized a photonic crystal fiber at the output stage of the laser to generate a supercontinuum of a wavelength range of 600 - 1100 nm. We analytically reveal laser parameter dependencies of photoacoustic signals. We test our microscopy system with a phantom made of horse hair, and present resultant images with point spread function of width 500 μm.

Keywords: Photoacoustics, photoacoustic microscopy, mode-locked, supercontiuum, fiber laser, pulse duration, beam width, pulse repetition frequency.

ÖZET

Fiber Lazer Tabanlı Geriye Modda Fotoakustik Mikroskopi Geliştirilmesi ve Görüntü Karakterizasyonu

İyonize ışın kullanmayan optik görüntüleme yöntemleri, sağlık endişelerinden dolayı diğer görüntüleme yöntemlerinin arasında popülerleşmeye başlamıştır. Ancak, salt optik methodların, ışığın saçılmasından dolayı derin doku görüntülemede eksiklikleri vardır. Fotoakustik görüntüleme ise bir yandan optik kontrastdan faydalanırken diğer yandan derin doku görüntülemede ultrasonun çözünürlüğüne ulaşması sebebiyle gelecek vaadeden bir yöntemdir. Fotoakustikte kullanılan lazerin atım süresi, atım sıklığı, ışın genişliği ve çıkış gücü gibi özellikleri oluşan sinyalin genliğinde, elde edilen görüntünün kalitesinde ölçülebilir etkilere sahiptir. Literatürde, mikroskopik ölçekte fotoakustik görüntülemede Q-anahtarlı lazerler, katı hal lazerleri ve fiber lazerler kullanılmaktadır. Kullanılan lazerlerin çoğu halihazırda piyasada bulunan ve özellikleri birbirinden bağımsız değiştirilemeyen lazerlerdir. Bizler bu çalışmada, özgün, tüm-fiberli mod-kilitli ve tamamen fotoakustik microskop gerekliliklerine göre tasarlanmış bir lazer sunuyoruz. Lazerin atım süresi 1 ile 3 ns arasında ayarlanabiliyorken atım sıklığı da 50 kHz ile 3.1 MHz arasında dijital olarak ayarlanabilmektedir. Tüm optik olayların fiberlerin içerisinde gerçekleşmesi, lazerin mekanik etkilere direncini arttırmakta ve kararlı bir yapıda olmasını sağlamaktadır. Lazerin çıkışında kullanılan fotonik-kristal fiber sayesinde 600 nm ile 1100 nm arasında sürekli ışın tayfı elde edilmektedir. Bu özgün çalışmada lazer özelliklerinin fotoakustik sinyalleri nasıl etkilediğini analitik olarak göstermekteyiz. Ürettiğimiz mikroskopi sistemini, at kıllarından oluşturulan fantomlar üzerinde deneyerek 500 μm noktasal yayılım fonksiyonu genişliğine sahip görüntüler oluşturduk.

Anahtar Sözcükler: Fotoakustik, fotoakustik mikroskop, mod kilitli lazer, fiber lazer, atım süresi, ışın genişliği, atım tekrar sıklığı.

TABLE OF CONTENTS

LIST OF FIGURES

LIST OF TABLES

LIST OF SYMBOLS

Δr	Minimum resolvable distance
I	Intensity of doughnut shape laser
I_S	Intensity of focused light
d_c	Characteristic dimension of heated region
v_s	Speed of sound
$p(\boldsymbol{r}, t)$	Pressure p at spherical coordinate $\boldsymbol{r}$ and time t
$T(\boldsymbol{r}, t)$	Temperature at position $\boldsymbol{r}$ and time t
C_V	Specific heat capacity at constant volume
H	Heating function
$H_t(t)$	Temporal component of heating function
$H_s(r)$	Spatial component of heating function
$p_0(\boldsymbol{r})$	Initial pressure rise
$S(\boldsymbol{r}, t)$	General notation for source term at position $\boldsymbol{r}$ and time t
$\tilde{F}(\omega)$	Fourier transform of a time series $f(t)$
$\mathcal{F}_t$	Fourier transform operator
$G(\boldsymbol{r}, \boldsymbol{r}'; t, t')$	Green's function in time domain
$\tilde{G}(\boldsymbol{r}, \boldsymbol{r}'; \omega)$	Green's function in frequency domain
R	Radius of spherical absorbing object
I_1	Temporary integral 1
I_2	Temporary integral 2
erf	Error function
sgn	Sign function
exp	Exponential function
λ	Wavelength of light
α_{th}	Thermal diffusivity
τ_{th}	Thermal relaxation time
τ_s	Stress relaxation time

β	Thermal coefficient of volume expansion
κ	Isothermal compressibility
ρ	Density of propagation medium
ω	Angular frequency
$\theta(r)$	Heaviside step function
μ	Absorption coefficient
$\delta(t)$	Dirac delta function

LIST OF ABBREVIATIONS

AlGaAs	Aluminium Gallium Arsenide
AOM	Acousto-optic Modulator
AR-PAM	Acoustic Resolution Photoacoustic Microscopy
CP	Coupler
DAQ	Data Acquisition
EM	Electromagnetic
FPALM	Fluorescent Photoactivation Localization Microscopy
FPGA	Field Programmable Gate Array
FWHM	Full Width Half Maximum
GUI	Graphical User Interface
HP-ISO	High Power Isolator
ISO	Isolator
IR	Infra Red Range of Spectrum
KTP	Potassium Titanyl Phosphate
LMA	Large Mode Area
NA	Numerical Aperture
Nd:Cr:YAG	Neodymium-doped Chromium-doped Yttrium Aluminum Garnet
Nd:YAG	Neodymium-doped Yttrium Aluminum Garnet
Nd:YLF	Neodymium-doped Yttrium Lithium Fluoride
NOLM	Non-linear Optical Loop Mirrors
NIR	Near Infra Red Range of Spectrum
OR-PAM	Optical Resolution Photoacoustic Microscopy
PA	Photoacoustic
PACT	Photoacoustic Computed Tomography
PAI	Photoacoustic Imaging
PAM	Photoacoustic Microscopy
PALM	Photoactivation Localization Microscopy
PCF	Photonic Crystal Fiber

PDL	Pump Diode Laser
POC	Polarization Controller
PPF	Pump Protection Filter
PRF	Pulse Repetition Frequency
PSF	Point Spread Function
SDK	Software Development Kit
SEM	Scanning Electron Microscopy
SIM	Structured Illumination Microscopy
SM	Single Mode
SMF	Single Mode Fiber
SNR	Signal to Noise Ratio
STED	Stimulated Emission Depletion
STORM	Stochastic Optical Reconstruction Microscopy
SW	Sub-wavelength
TEM	Transverse Electro-magnetic
VIS	Visible Range of Spectrum
WDM	Wavelength Division Multiplexer
Yb-DF	Yttirbium-doped Fiber

1. Introduction

Both in conventional light microscopy and relatively novel techniques as two photon microscopy and confocal microscopy resolutions are limited to Abbe's diffraction limit [1, 2]. For any microscopic imaging modality, minimum resolvable distance d is calculated as

$$d = \frac{\lambda}{2 \times \mathrm{NA}} \tag{1.1}$$

where λ is the wavelength of the light, and NA is the numerical aperture of the objective used to focus the light onto the specimen. Roughly, the distances between two distinguishable objects are equal to the half of the wavelength. Since de Broglie wavelength of an electron comparably shorter then the light, scanning electron microscopy (SEM) achieves much higher resolution. Nevertheless, SEM is not very practical for biological imaging due to electron interaction with sample itself and low penetration depth [1]. Although fluorescence microscopy techniques achieved relatively higher resolutions, they still are not able to overcome Abbe's diffraction limit [1].

In 1994, Hell and Wichmann developed a novel laser scanning fluorescence microscopy technique [3]. They broke diffraction limit and reduced the size of point spread function (PSF) by utilizing a second doughnut shape laser to create a stimulated fluorescence emission in that outer region of the focal spot. This technique was named as stimulation emission depletion (STED) microscopy.

In STED microscopy, the wavelength of the second laser is greater; thus, stimulated emission is not detected by the detector and PSF is sharpened to a much smaller area. Eq. 1.2 represents minimum distinguishable distance for a STED microscope

$$\Delta r \sim \frac{\lambda}{2\mathrm{NA}\sqrt{1 + \frac{I}{I_S}}} \tag{1.2}$$

where Δr is minimum resolvable distance, λ is the wavelength of focused light, I is the intensity of doughnut shape laser and I_S is the intensity of the focused light. Although there seems no theoretical limit for the resolution of STED microscope, laser photodamage safety limit creates a practical boundary [1]. Around a 10 nm resolution [2] is achieved in STED microscopy by using hundreds of milliwatts power lasers. Additional to sharpening of PSF, estimation of center of a PSF further improves the resolution. The mathematical process of estimating the location of the source that creates PSF is named as pointillism [2, 4].

Concurrently with the development of STED microscopy, three different groups launched single fluorophore localization based super-resolution microscopy techniques [1]. Photo-activated localization microscopy (PALM) [5], stochastic optical reconstruction microscopy (STORM) [6], and fluorescence photo-activated localization microscopy (FPALM) [7] are three different names of similar techniques.

Those three methods utilize photoactivatable fluorescent labels while estimating the center of the PSFs. Randomly switching activated molecules increases the probability of single molecule activation per image. Then combination of all frames creates a individual image [1, 2].

Structured illumination microscopy (SIM) relies on a simple concept of moire pattern, which is an interference pattern of two overlying grids with a different angle or mesh sizes. If the pattern of light is known, unknown pattern can be extracted from the resultant image. As the frequency of known pattern increases, achieved resolution also increases. However, the frequency of known pattern is also limited to Abbe's diffraction limit [1]. It is possible to achieve 125 nm lateral resolution and 250 nm axially resolution in SIM [2, 8].

Although super-resolution microscopy is very promising for *ex vivo* operation, it suffers from the depth of resolution due to mean free path of light of 1 mm [9]. Being able to image tumor cells *in vivo* would accelerate especially animal studies and be promising in cancer research. Since tumorous tissues have comparably large number of vessels with respect to healthy tissue, they create high optical contrast in visible and near infrared region.

Photoacoustic microscopy (PAM) becomes essential to satisfy the need for *in vivo* studies. In PAM, the main source of signals is absorption of light. Ignoring the impact of scattering becomes a reasonable assumption while creating a model resembling photoacoustic imaging (PAI). Whether the light is scattered or not it is important light to be absorbed. Moreover, in photoacoustic imaging detection is acoustic, and scattering of ultrasound in soft tissue is weak. In other words, PAM utilizes optical absorption contrast and ultrasonic resolution in order to realize *in vivo*, deep tissue imaging. By choosing optimum parameters depending on the application, it is possible to image from organ to organelle level as seen in Figure 1.1.

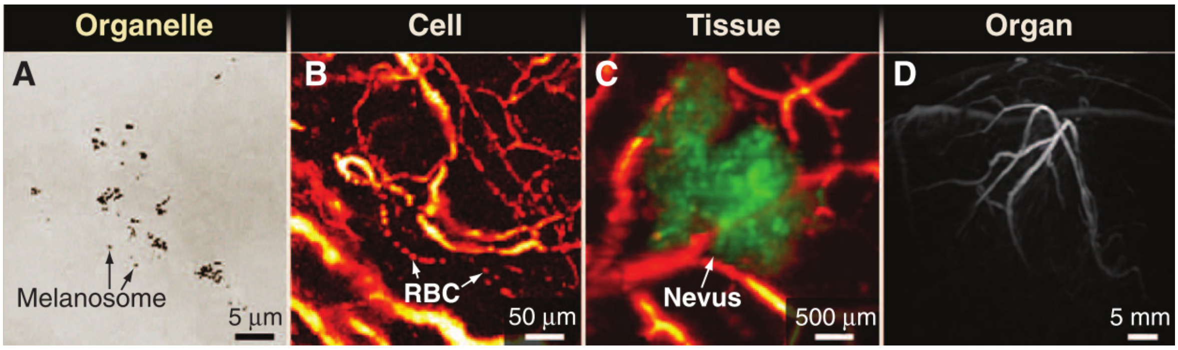

Figure 1.1 Photoacoustic images from organelles to organs [10]. *"(A) Subwavelength (SW) PAM of melanosomes in the ear of a black mouse. (B) OR-PAM of individual red blood cells traveling along a capillary in a mouse ear. (C)acoustic resolution photoacoustic microscopy (AR-PAM) of a nevus on a human fore arm.(D)PA computed tomography (PACT) of a human breast."*

Based on the previous studies on photoacoustic microscopy and other microscopy techniques, we compare image performances and tabulate in Table 1.1. For each property, typical value and best value is given on sequential rows. The compared features and corresponding values for fluorescence microscopy are adopted from review paper of Toomre et al. [2]. The values on the photoacoustic microscopy column are taken from review paper of Wang et al. [10]. However, the typical and the best values of resolution imaging depth do not concurrently occurs in PAM. There is a trade of between depth of imaging and resolution.

Table 1.1
Comparison table of super-resolution microscopy methods and photoacoustic microscopy [2, 10].

	Confocal	SIM	STED	(F)PALM/STORM	PAI
xy - resolution	200 - 250 nm	100 nm	25 - 80 nm	25 - 40 nm	5 μm [11]
		130 nm	$<$ 10 nm	10 nm	500 nm [12]
z - resolution	500 - 700 nm	250 nm	150 - 600 nm	25 - 40 nm	15 μm [11]
		200 nm	30 nm	10 nm	5 μm
Depth (max)	5 - 20 μm	5 μm	5 μm	25 - 40 nm	100 μm [11]
	$>$50 μm	20 μm	20 μm	10 nm	3 mm [13]
Live Cell	good	poor	poor	poor	excellent

1.1 Photoacoustics

Photoacoustic effect is first proposed by Alexander Graham Bell, in 1880 [14]. He discovered that, some matters emits sound if they are illuminated with light. Engineering of photoacoustic effect came across after 1970s [15, 16] in material testing, gas tank analysis [17]. Most of the physics beyond photoacoustics was investigated during that period. However, most of the models were generated for homogeneous materials (solids, liquids and gases) and applied to material testing. For biomedical and biological applications, on the other hand, photoacoustics is relatively new and has just passed its infant period during the last decade.

Lihong Wang's research group made beneficial contributions to the biomedical photoacoustics and photoacoustic imaging fields. They published in the very wide range of photoacoustic imaging, from organs to organelle scale [18, 10].

Vasilis Ntziachristos' opto-acoustics laboratory utilizes AR-PAM for animal imaging. They investigate contrast agents for photoacoustic imaging and uses them in multispectral optoacoustic imaging [19]. They also try to develop novel clinical applications of photoacoustic imaging [20].

Photoacoustic imaging attracts different groups in the field of biomedical imaging, due to its low cost, non-invasiveness and ability to image *in vivo*.

1.1.1 Photoacoustic Wave Generation

This thesis approaches photoacoustics concept from the biomedical perspective and declares PA wave generation in biological tissue. Our wave generation model includes additional assumptions to the models developed for non-destructive testing of metals. For example, electromagnetic radiation absorption is not limited with only the surface of the sample as in metals and heat conduction can be disregarded [21]. For the last decade, biomedical photoacoustics created a widely accepted and simpler model based on its own assumptions specific to biomedical application. When a pulsed light is illuminated on a tissue sample, there occurs two independent events during propagation of light in tissue: Absorption and scattering. As mentioned in Section 1.1, only absorption is assumed to play a role in photoacoustic wave generation. Scattering may result absorption of energy in undesired locations; therefore, may end up interference to photoacoustic signals. However, due to their low amplitudes and out of focus locations this interference acoustic signals are naturally filtered out by transducers.

The absorbed light transfers its energy into the medium as heat and causes a local temperature rise on the order of milli-Kelvins [22]. As it is seen in Figure 1.2, the local temperature rise in the absorber triggers a local thermoelastic expansion and compression around absorber.

For an effective photoacoustic wave generation, pulse duration should be much shorter than the time required for thermal diffusion and stress relaxation [18]. Those two conditions are named as thermal confinement and stress confinement. Thermal relaxation time is estimated as

$$\tau_{th} = \frac{d_c^2}{\alpha_{th}} \tag{1.3}$$

where d_c is characteristic dimension of heated region (minimum of illuminated region

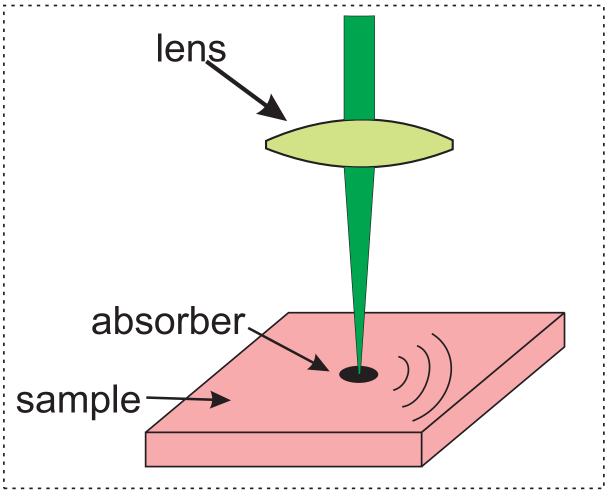

Figure 1.2 Illustration of photoacoustic wave generation mechanism.

or absorbed region) and α_{th} is thermal diffusivity (m^2/s). Stress relaxation time calculated as

$$\tau_s = \frac{d_c}{v_s} \tag{1.4}$$

where v_s denotes for acoustic speed [9].

Initially generated pressure wave propagates through sample and arrives ultrasonic transducers. Photoacoustic wave in any time and in any space coordinate obeys the following wave equation

$$(\nabla^2 - \frac{1}{v_s^2}\frac{\partial^2}{\partial t^2})p(\boldsymbol{r},t) = -\frac{\beta}{\kappa v_s^2}\frac{\partial^2 T(\boldsymbol{r},t)}{\partial t^2} \tag{1.5}$$

where v_s is acoustic propagation speed, $p(\boldsymbol{r},t)$ is pressure wave in time t and space coordinate r, β is the thermal coefficient of volume expansion, κ is the isothermal compressibility, and $T(\boldsymbol{r},t)$ is temperature at position $\boldsymbol{r}$ and time t [18].

For a short laser pulse, thermal equation may be represented by a heating function as it follows

$$\rho C_V \frac{\partial T(\boldsymbol{r},t)}{\partial t} = H(\boldsymbol{r},t) \tag{1.6}$$

where H is the heating function, the amount of heat generated by light absorption per unit volume and per unit time, ρ denotes density and C_V denotes specific heat capacity at constant volume [18].

Reordering Eq. 1.6 and substituting $T(\boldsymbol{r},t)$ into Eq. 1.5 we get

$$(\nabla^2 - \frac{1}{v_s^2}\frac{\partial^2}{\partial t^2})p(\boldsymbol{r},t) = -\frac{\beta}{C_P}\frac{\partial H(\boldsymbol{r},t)}{\partial t}. \tag{1.7}$$

The solution to the photoacoustic wave equation can be obtained by the well-known Green's function method. [23, 9] By assuming the source term that is a combination of spatial and temporal profiles represented by the Dirac delta distributions, a time domain solution is obtained by Lihong Wang [9, 18]. A detailed solution for Dirac delta source is given in Appendix A. For an optically absorbing spherical object, treating temporal profile as Gaussian, we solve the photoacoustic wave equation analytically via the Fourier transform for rectangular radial profile and obtain frequency domain solutions. Later, carrying out inverse Fourier transform, we also obtain exact time domain solutions without any approximation except the azimuthal symmetry. We previously published the calculations in the following part as proceedings [24]. Our results are obtained analytically and more comprehensive compared to the previous works in literature. We confirm our results by plotting the photoacoustic signals as a function of time for different radial positions outside the spherical object for realistic values of photoacoustic parameters.

The right hand side of Eq. 1.7 is the source term of wave equation. We can regard source term as

$$S(\boldsymbol{r},t) \equiv -\frac{\beta}{C_P}\frac{\partial H(\boldsymbol{r},t)}{\partial t} \tag{1.8}$$

and the heating function can be decomposed into spatial and temporal components as $H(\boldsymbol{r},t) = H_s(\boldsymbol{r})H_t(t)$. Here, temporal component is assumed to has Gaussian shape,

$$H_t(t) = \frac{1}{\sqrt{2\pi\sigma^2}}\exp(-\frac{t^2}{2\sigma^2}) \tag{1.9}$$

with σ is the standard deviation of Gaussian distribution or also may be considered as pulse duration of the laser.

The initial pressure rise just after the pulse, $p_0(\boldsymbol{r})$, can be written as [18, 9]

$$p_0(\boldsymbol{r}) = \frac{\beta T(\boldsymbol{r})}{\kappa}. \tag{1.10}$$

Assuming that all the absorbed electromagnetic energy is converted into heat and non-thermal relaxation is ignored, the temperature rise can be expressed by

$$T(\boldsymbol{r}) = \frac{H_s(\boldsymbol{r})}{\rho C_V}. \tag{1.11}$$

Combining Eq. 1.10 with Eq. 1.11 and writing

$$\kappa = \frac{C_P}{\rho v_s^2 C_V}, \tag{1.12}$$

we get spatial component of source as

$$H_s(\boldsymbol{r}) = \frac{p_0(\boldsymbol{r})}{v_s^2} \frac{C_P}{\beta}. \tag{1.13}$$

Substituting Eq. 1.9 and Eq. 1.13 into Eq. 1.8 leads to

$$S(\boldsymbol{r}, t) = -\frac{p_0(\boldsymbol{r})}{v_s^2} \frac{\partial}{\partial t} \left(\frac{1}{\sqrt{2\pi\sigma^2}} \exp(-\frac{t^2}{2\sigma^2}) \right). \tag{1.14}$$

Using Fourier and inverse Fourier convention as

$$\tilde{F}(\omega) = \frac{1}{\sqrt{2\pi}} \int_{-\infty}^{\infty} p(\boldsymbol{r}, t) \exp(-i\omega t) dt \tag{1.15}$$

and

$$f(t) = \frac{1}{\sqrt{2\pi}} \int_{-\infty}^{\infty} \tilde{F}(\boldsymbol{r}, \omega) \exp(i\omega t) d\omega \tag{1.16}$$

respectively. Fourier transform of $S(\boldsymbol{r}, t)$ gives

$$\begin{aligned} \tilde{S}(\boldsymbol{r}, \omega) &= -\frac{p_0(\boldsymbol{r})}{v_s^2} i\omega \mathcal{F}_t \left(\frac{1}{\sqrt{2\pi\sigma^2}} \exp(-\frac{t^2}{2\sigma^2}) \right) \\ &= i\omega \frac{p_0(\boldsymbol{r})}{v_s^2} \frac{1}{\sqrt{2\pi}} \exp(-\frac{\sigma^2\omega^2}{2}) \end{aligned} \tag{1.17}$$

where $\mathcal{F}_t$ denotes for Fourier transform operator of a time series.

The photoacoustic wave equation can be expressed in frequency domain by using the Fourier convention declared in Eq. 1.15 and in Eq. 1.16. Here the frequency domain photoacoustic wave equation is expressed as

$$\nabla^2 \tilde{p}(\boldsymbol{r},\omega) + \frac{\omega^2}{v_s^2}\tilde{p}(\boldsymbol{r},\omega) = i\omega\frac{p_0(\boldsymbol{r})}{v_s^2}\exp(-\frac{\sigma^2\omega^2}{2}) \tag{1.18}$$

where i is complex number and ω is angular frequency domain.

The Green's function of Eq. 1.18 is given by the following expression [23]

$$\tilde{G}(\boldsymbol{r},\boldsymbol{r'};\omega) = -\frac{1}{4\pi \mid \boldsymbol{r}-\boldsymbol{r'} \mid}\exp(i\frac{\omega}{v_s} \mid \boldsymbol{r}-\boldsymbol{r'} \mid) \tag{1.19}$$

where the Green's function is an outgoing spherical wave for $\mid \boldsymbol{r}-\boldsymbol{r'} \mid \to \infty$.

The solution in ω domain can be found by evaluating the following integral

$$\tilde{p}(\boldsymbol{r},\omega) = \int \tilde{G}(\boldsymbol{r},\boldsymbol{r'};\omega)\tilde{S}(\boldsymbol{r'};\omega)d^3r^{'}. \tag{1.20}$$

Substituting Eq. 1.17 and Eq. 1.19 into Eq. 1.20 gives

$$\tilde{p}(\boldsymbol{r},\omega) = -\frac{i}{4\pi}\frac{\omega}{v_s^2}\exp(-\frac{\sigma^2\omega^2}{2})\int p_0(r^{'})\frac{\exp(i\frac{\omega}{v_s} \mid \boldsymbol{r}-\boldsymbol{r'} \mid)}{\mid \boldsymbol{r}-\boldsymbol{r'} \mid}d^3r^{'}. \tag{1.21}$$

When a spherical object of radius R is excited by a short pulsed laser beam, the initial pressure p_0 is created inside the object so that the initial pressure distribution can be written as [9, 18]

$$p_0(r) = p_0\theta(r)\theta(-r+R) \tag{1.22}$$

where θ is the Heaviside step function.

Hence, writing Eq. 1.22 into Eq. 1.21 and simplifying the geometry as taking $\boldsymbol{r}$

along z axis, we get

$$\tilde{p}(\boldsymbol{r},\omega) = -p_0 \frac{i}{4\pi}\frac{\omega}{v_s^2}\exp(-\frac{\sigma^2\omega^2}{2})\int_0^{2\pi} d\phi' \int_0^R r'^2 dr' \int_{-1}^{1} d\mu' \frac{\exp(i\frac{\omega}{v_s} \mid \boldsymbol{r}-\boldsymbol{r'} \mid)}{\mid \boldsymbol{r}-\boldsymbol{r'} \mid} \quad (1.23)$$

where $\mu' = \cos\theta'$ and $\mid \boldsymbol{r}-\boldsymbol{r'} \mid = \sqrt{r^2 - 2rr'\mu' + r'^2}$.

The solution of the innermost integral is found as

$$\int_{-1}^{1} d\mu' \frac{e^{(i\frac{\omega}{v_s}\sqrt{r^2-2rr'\mu'+r'^2})}}{\sqrt{r^2-2rr'\mu'+r'^2}} = -\frac{1}{irr'\frac{\omega}{v_s}}[e^{(i\frac{\omega}{v_s}(r-r'))} - e^{(i\frac{\omega}{v_s}(r+r'))}]. \quad (1.24)$$

Substituting Eq. 1.24 into Eq. 1.23, then taking integrals over remaining two dimension yields ω domain solution as

$$\tilde{p}(r,\omega) = ip_0\frac{v_s}{r}\frac{\exp(-\frac{\sigma^2\omega^2}{2}+i\frac{\omega}{v_s}r)}{\omega^2}[\frac{\omega}{v_s}R\cos(\frac{\omega}{v_s}R) - \sin(\frac{\omega}{v_s}R)] \quad (1.25)$$

where $r > R$ or $r > r'$.

Inverse Fourier transform of $\tilde{p}(r,\omega)$ results as

$$p(r,t) = \frac{i}{\sqrt{2\pi}}p_0\frac{v_s}{r}\int_{-\infty}^{\infty}\frac{\exp(-\frac{\sigma^2\omega^2}{2}+i\frac{\omega}{v_s}r - i\omega t)}{\omega^2}[\frac{\omega}{v_s}R\cos(\frac{\omega}{v_s}R) - \sin(\frac{\omega}{v_s}R)]d\omega. \quad (1.26)$$

Writing $\cos(\frac{\omega}{v_s}R)$ and $\sin(\frac{\omega}{v_s}R)$ in terms of exponentials into Eq.(1.26) gives

$$\begin{aligned} p(r,t) &= \frac{ip_0}{2\sqrt{2\pi}}\frac{R}{r}\int_{-\infty}^{\infty}\{\frac{e^{-\frac{\sigma^2\omega^2}{2}+i\omega(\frac{r+R}{v_s}-t)}}{\omega} + \frac{e^{-\frac{\sigma^2\omega^2}{2}+i\omega(\frac{r-R}{v_s}-t)}}{\omega}\}d\omega \\ &+ \frac{p_0}{2\sqrt{2\pi}}\frac{v_s}{r}\int_{-\infty}^{\infty}\{\frac{e^{-\frac{\sigma^2\omega^2}{2}+i\omega(\frac{r+R}{v_s}-t)}}{\omega^2} - \frac{e^{-\frac{\sigma^2\omega^2}{2}+i\omega(\frac{r-R}{v_s}-t)}}{\omega^2}\}d\omega. \quad (1.27) \end{aligned}$$

If the following I_1 and I_2 integrals are solved, then the solution of the photoacoustic equation can be obtained

$$I_1 = \int_{-\infty}^{\infty}\frac{\exp[-\frac{\sigma^2\omega^2}{2}+i\omega(\frac{r+R}{v_s}-t)]}{\omega}d\omega, \quad (1.28)$$

$$I_2 = \int_{-\infty}^{\infty} \frac{\exp[-\frac{\sigma^2\omega^2}{2} + i\omega(\frac{r+R}{v_s} - t)]}{\omega^2} d\omega. \tag{1.29}$$

Calculation of these I_1 and I_2 integrals is possible with the residue theorem[23]. Jordan's lemma states that if $f(z) \to 0$ as $z \to \infty$, then

$$\lim_{R\to\infty} \int_{C_R} f(z) e^{i\alpha z} dz = 0 \tag{1.30}$$

where C_R is a circular path of infinite radius on the upper z plane for $\alpha > 0$. Reordering the terms in the integral in Eq. 1.28 to the form of the integral in Eq. 1.30 we get

$$\begin{aligned} \oint \frac{e^{-\frac{\sigma^2\omega^2}{2}}}{\omega} e^{i\omega(\frac{r+R}{v_s}-t)} d\omega = \lim_{R\to\infty} & \int_{C_R} \frac{e^{-\frac{\sigma^2\omega^2}{2}}}{\omega} e^{i\omega(\frac{r+R}{v_s}-t)} d\omega \\ + & \int_{-\infty}^{\infty} \frac{e^{-\frac{\sigma^2\omega^2}{2}}}{\omega} e^{i\omega(\frac{r+R}{v_s}-t)} d\omega. \end{aligned} \tag{1.31}$$

For $(\frac{r+R}{v_s} - t) > 0$, first integral of the right hand side becomes zero and left hand side can be calculated by applying residue theorem for pole $\omega = 0$.

$$\oint \frac{e^{-\frac{\sigma^2\omega^2}{2}}}{\omega} e^{i\omega(\frac{r+R}{v_s}-t)} d\omega = \begin{cases} \pi i \lim_{\omega\to 0}(\omega \frac{e^{-\frac{\sigma^2\omega^2}{2}}}{\omega} e^{i\omega(\frac{r+R}{v_s}-t)}) & \text{if}(\frac{r+R}{v_s} - t) > 0, \\ -\pi i \lim_{\omega\to 0}(\omega \frac{e^{-\frac{\sigma^2\omega^2}{2}}}{\omega} e^{i\omega(\frac{r+R}{v_s}-t)}) & \text{if}(\frac{r+R}{v_s} - t) < 0. \end{cases} \tag{1.32}$$

By adopting same approach, I_1 and I_2 can be calculated as

$$I_1 = \pi i \,\mathrm{sgn}\,(\frac{r+R}{v_s} - t) \tag{1.33}$$

and

$$I_2 = -\pi(\frac{r+R}{v_s} - t) \,\mathrm{sgn}\,(\frac{r+R}{v_s} - t). \tag{1.34}$$

Substituting solutions Eq. 1.33 and Eq. 1.34 into corresponding integral forms in Eq. 1.27 yields the following solution of photoacoustic equation in time domain for a spherical object homogeneously heated by a short laser pulse having a Gaussian temporal profile

$$p(r,t) = \frac{1}{2}\sqrt{\frac{\pi}{2}} \frac{p_0}{r} [(r - v_s t) \,\mathrm{sgn}(\frac{r+R}{v_s} - t) + (-r + v_s t) \,\mathrm{sgn}(\frac{r-R}{v_s} - t)]. \tag{1.35}$$

There are three cases based on the propagation time when observation point is outside the spherical object [18, 25]:

- If $r - R > v_s t$, the spherical object does not intersect with the spherical shell of radius $v_s t$ which is centered at the observation point so that $p(r, t)$ becomes zero.
- If $v_s t$ is between the interval $[r - R, r + R]$, the heated spherical object touches the spherical shell of radius $v_s t$. Therefore, the pressure can be described by Eq. (1.35).
- If $r + R < v_s t$, then the spherical object cannot intersect with the spherical shell; thus, $p(r, t)$ becomes zero.

Therefore, these three cases can be combined into the following expression by utilizing the Heaviside step function, $\theta(x)$,

$$\begin{aligned} p(r,t) = \quad & \frac{1}{2}\sqrt{\frac{\pi}{2}}\frac{p_0}{r}\{(r - v_s t)\,\mathrm{sgn}(\frac{r+R}{v_s} - t) + (-r + v_s t)\,\mathrm{sgn}(\frac{r-R}{v_s} - t)\} \\ & \times\theta(r- \mid R - v_s t \mid)\theta(-r + R + v_s t) \end{aligned} \tag{1.36}$$

for outside the object $(r > R)$.

Note that the solution still does not contain a term for pulse duration. Mathematical assumptions during contour integral solution leads us to this solution. Figure 1.3 shows that the change of the normalized photoacoustic pressure wave $\frac{p(r,t)}{p_0}$ with respect to normalized time $\frac{v_s t}{R}$ for Gaussian temporal and rectangular radial profiles observed at different radial positions.

The only variable in the final expression of $p(r, t)$ is the initial pressure p_0. The initial pressure amplitude is dependent on laser parameters and the following subsection investigated this relation.

1.1.1.1 Photon Fluence. PA wave equation actually deals with time after initial pressure wave is generated. Assumption of stress and thermal confinement relieves the

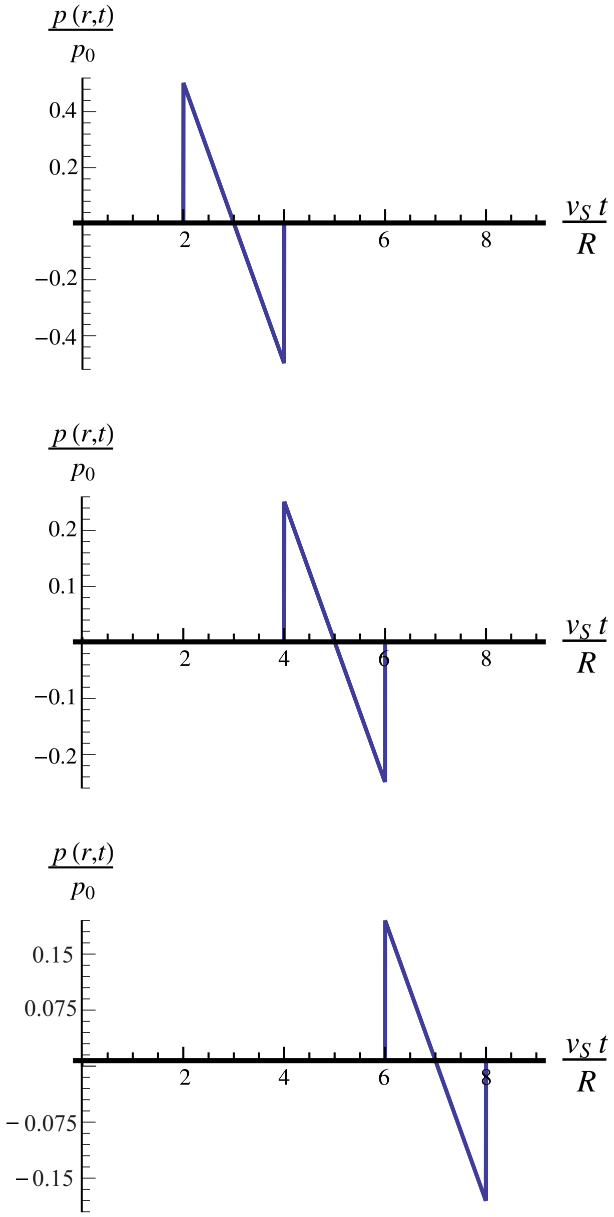

Figure 1.3 Normalized photoacoustic pressure wave $\frac{p(r,t)}{p_0}$ vs. normalized time $\frac{v_s t}{R}$ for Gaussian temporal and rectangular radial profiles observed at different radial positions (a) $r = 2R$ (b) $r = 4R$ (c) $r = 6R$ [24].

concerns about initial wave generation. The initial wave generation is directly related with photon fluence.

Photon fluence (flux) is defined as the number of photons passing through a unit area and causes a proportional optical energy flow per unit surface area. Although it is trivial to calculate fluence on the surface of the sample, the fluence calculation for a deeper regions of a turbid medium requires more complicated estimation models.

In literature, there are gold standard methods that give realistic fluence models in a biological tissue. Diffusion approach, radiation transport equation solution are main analytic methods to obtain photon flux in tissue. In addition to analytic models, Markov Chain Monte Carlo simulations give numerical results that perfectly match with real photon distribution in tissue.

For *ex vivo* microscopic imaging, the thickness of specimen is small enough to ignore light propagation in tissue. Photon fluence can approximately computed as in the surface of the tissue. For *in vivo* imaging purposes, assuming a constant attenuation of light energy gives reasonable result for depth less than a centimeter.

In order to generate detectable PA waves, energy fluence has to reach a sufficient level. Thus, the beam diameter and the average power of laser acts contrarily. In AR-PAM, weakly focused or diffused light is used [26, 27]. The use of large beam diameter allows higher pulse energies with same fluence. Hence, the laser light reaches a deeper region of tissue without damaging the surface of the specimen.

1.1.1.2 Radial Profile of Laser. Radial profile of the laser describes the intensity distribution of light in space domain. From electromagnetic (EM) phenomena point of view, it is the amplitude of the EM wave depending on space coordinates x, y, z. If a transverse wave travelling in $+z$ direction is assumed then radial profile can be denoted as $I(x, y)$. Considering the optical waveguides and wave theory, it is logical to assume transverse electromagnetic zero-zero mode (TEM_{00}) [28, 29]. TEM_{00} mode ensures spatial coherence, and it is the lowest order mode, resembles a Gaussian distributed intensity at the output [30].

For a Gaussian laser beam, the beamwidth (equivalently named as focal spot size) is expressed as full width half maximum (FWHM), which is proportional to standard deviation of the Gaussian. If a two dimensional symmetrical Gaussian is assumed and center of beam is assumed at origin, the intensity of laser can be expressed as

$$I(r) = \frac{1}{s\sqrt{2\pi}} \exp -\frac{r^2}{2s^2} \tag{1.37}$$

where r is the distance from the center of beam on the transverse plane and s is the standard deviation of Gaussian.

Beamwidth of the light determines the spatial resolution of photoacoustic image. For the case that focal spot size is greater than the cross section of absorbing object on the imaging plane, as seen in Figure 1.4, simultaneously generated pressure waves overlap as coming from single object. As a result, the two absorber illuminated by a single Gaussian beam are not resolvable.

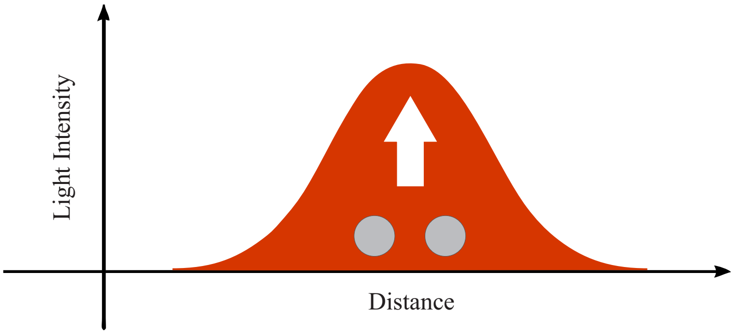

Figure 1.4 For large Gaussian, objects closer than FWHM are not resolvable.

For the case of a significantly narrow beamwidth, photoacoustic wave generation occurs locally in the illuminated segment of absorber. As seen in Figure 1.5, Gaussian beam generates PA waves when they coincide with absorber. If laser pulse hits outer region of absorber, it does not create a detectable PA wave. In that case, the limiting factor of lateral resolution becomes the scanning sensitivity of the system.

If the focal spot size is smaller than the cross section of absorbing object on the imaging plane, this also affects the ultrasound frequency. Similar to the physics of transducers, the thickness or the size of active material (absorbing volume for PAI) is inversely proportional to the frequency of the generated ultrasound wave. Hence, to

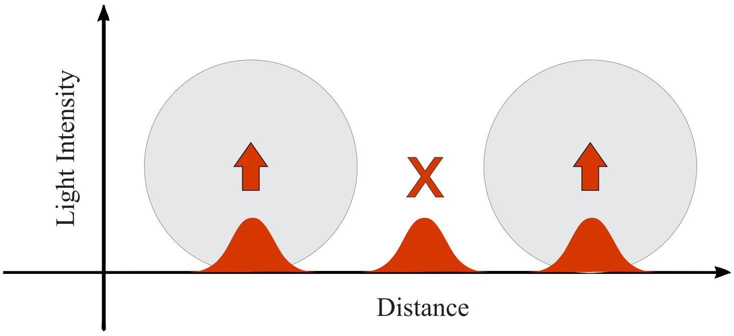

Figure 1.5 For small Gaussian, limiting factor for resolution is scan step size.

achieve higher resolution in photoacoustic imaging it is important to select appropriate focal spot size, scanning resolution and ultrasound transducer frequency.

1.1.1.3 Pulse Repetition Frequency.

Pulse repetition frequency (PRF) of a laser is an important parameter in terms of fast image acquisition. Although it depends on intrinsic properties of the laser used, it has some limitations due to the nature of PAI.

The speed of sound in biological tissues ($\tilde{1}.5$ mm/μsec) and in water ($\tilde{1}.4$ mm/μsec), limits the minimum time between two consecutive pulses. The pulses should hit the tissue in such a period that allows acoustic waves travel out of the focal spot. Moreover, the distance that ultrasound waves travel inside the water tank is also important. Assuming that transducer surface is 7.5 mm away from the sample, we calculate time delay as 5 μsec, which yields a maximum 200 kHz PRF.

Additional to temporal resolution consideration, PRF of a pulsed laser determines the energy per pulse value. Intuitively, the constant power delivered by the pump during amplification of light is distributed to each pulse. If the number of pulses in a certain duration increases, then the energy share of each pulse decreases. Mathematically, the relation between energy and PRF is formulated as [31],

$$P_{pump} = E_{pp} f_{pr} \tag{1.38}$$

where P_{pump} is the average power delivered by a pump source, E_{pp} is the energy per-pulse, and f_{pr} is pulse repetition frequency.

High PRF is desirable for video rate imaging; however, there are other factors that limit achievable PRF. Depending on the sample and device set up, one should choose optimum value for PRF by considering the trade off between speed and energy.

1.1.1.4 Wavelength. When a light is incident on a matter, there occurs an electromagnetic energy transfer to the matter. Depending on the natural frequency of the electromagnetic wave and the energy levels of the matter, the type of energy transfer vary. For infrared and near infrared spectrum, main transfer mechanism relies on atomic vibrational energy. When infrared radiation is incident upon a sample, the amplitude of vibration will increase drastically due to resonance [32]. From a larger scale, overall effect of absorption is attenuation in the intensity of the light beam propagating through a medium. Famous Lambert's law states that output beam intensity is exponentially dependent on propagation distance through the sample and absorption coefficient. It is formulated as

$$I_{out} = I_{in} e^{\mu_a d} \tag{1.39}$$

where I_{out} denotes for output light intensity I_{in} denotes for incident light intensity and μ_a denotes absorption coefficient and d denotes the distance that light propagates.

In photoacoustic imaging, the source of contrast is the absorption coefficient difference between an absorber and the surrounding tissue. Hence, wavelength dependent μ_a plays a crucial role in imaging performance. Larger differences of absorption coefficients yield a better resolution.

Absorption coefficient of a biological tissue is highly dependent on the composition of that tissue. There are various chromophores in a tissue and the percentage of that chromophores defines the overall absorption coefficient. Three main chromophores are water, blood and fat.

In 1973, Hale et al. [33] made experimental measurements and obtained wavelength dependent absorption coefficient of water. The spectral bandwidth (200 nm - 200 μm) they used was very large compared to the visible and the near infrared (VIS-NIR) region. In 1997, Pope et al. zoomed into the spectrum and obtained more detailed measurements from 340 nm to 700 nm [34, 35].

Figure 1.6 shows the absorption spectra of the water. Until 900 nm, water absorption is not significant. After 900 nm, the absorption coefficient increases sharply and makes a peak at 980 nm region [36]. Comparing to other chromophores, VIS-NIR window is the transparent spectrum for water and allows deep imaging.

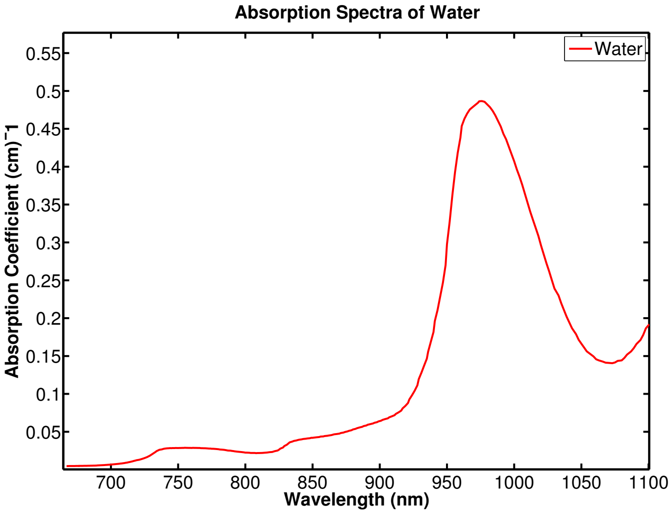

Figure 1.6 Specific absorption spectra of water. (Data is retrieved from website of Oregon Medical Laser Center) [36].

In the range of the window of transparency for water, oxyhemoglobin (HbO2) and deoxyhemoglobin (Hb) are most dominant absorbers of NIR light. The specific absorption spectra of hemoglobin is studied by Cope et al. [37]. There exist a significant difference of absorption coefficients, particularly in the region starting from red light ends at NIR. Figure 1.7 shows wavelength dependent values of molar absorption coefficient of hemoglobin [38, 39].

Another main component of biological tissue is fat and mammalian fat is mostly composed of triglyceride. The specific absorption coefficient of pork fat (lipid) be-

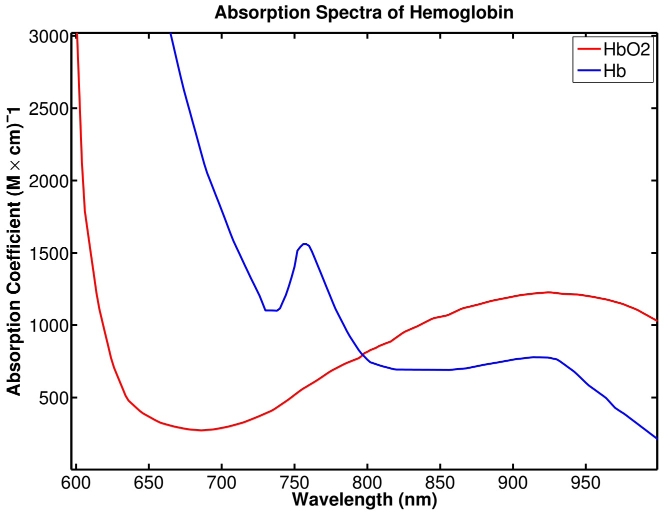

Figure 1.7 Molar absorption spectra of oxyhemoglobin and deoxyhemoglobin. (Data is retrieved from website of Oregon Medical Laser Center) [39].

tween 800 nm and 1080 nm wavelength is experimentally studied by Conway et al. in 1984 [40]. In 2004, van Veen et al. expanded the wavelength range to the spectrum 430 nm - 1100 nm [41]. Figure 1.8 shows the absorption spectrum of lipid [41]. Additional to water, blood (specifically hemoglobin), and lipid, there are different chromophores like melanin, cytochrome C-oxidase enzyme [37].

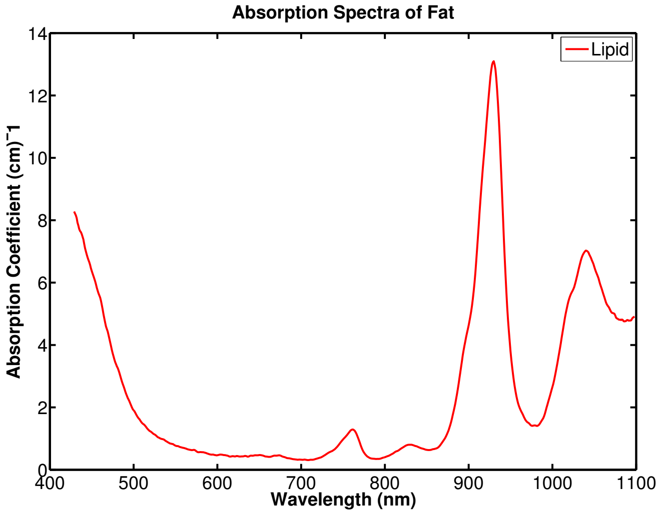

Figure 1.8 Specific absorption spectrum of lipid [41].

The utilization of a chromophore strongly depends on the difference of absorption coefficients at a certain wavelength. This creates optical contrast and allows photoacoustic imaging possible for certain applications. For example, imaging of cancerous tumors, where tissue is surrounded with excessive capillaries, it is consistent to use the wavelength, at where hemoglobin absorption is maximum and water absorption is minimum. Thus, 532 nm (second harmonic of 1064 nm IR light) can be considered as optimum wavelength. However, if tissue oxygenation is important, then NIR region around 880 nm is a better region evaluating the specific absorptions.

1.1.1.5 Laser Pulse Duration. Pulse duration of laser excitation is a crucial parameter in photoacoustic imaging since it affects the amplitude of generated pressure. The higher the initial pressure yields a greater signal to noise ratio (SNR). For an efficient PA generation, pulse duration should be on the order of nanoseconds. Considering the speed of sound in tissue and stress relaxation speed we can conclude that all the other dynamics of thermoelastic expansion like heat diffusion are observed as steady state during laser illumination. However, for the pulse duration on the order of microseconds, heat diffusion should be taken into account. This makes physical model beyond PA more complicated. Solving a heat diffusion equation is required additional to particle displacement or pressure wave equation.

1.2 Motivation

In literature, the pulse duration dependency is analyzed by convolving a square shape pulse of certain width with the Dirac delta solution [42, 43]. Karabutov et al. solved PA wave equation and obtained a general expression that depends on dimensionless parameters denoted as A and D. They analysed PA wave for both very short pulse duration ($A << 1$, $D << 1$) and long pulse duration ($A >> 1$, $D >> 1$) [42].

Sigrist et al. generated a model for spatially Gaussian source problems; however, their model does not include temporal distribution of source [44]. Lai *et al.* proposed a theoretical method for pulsed optoacoustics for a weakly absorbing liquid [45]. They investigated laser beams with Gaussian shaped temporal and radial profiles. Using far field approximation, they obtained analytic and numerical results. Hoelen *et al.* [46] modified Sigrist's solution [44] and represented pressure distribution in terms of parameters of Gaussian spatiotemporal source formation. They examined the solution for three different absorber geometries in all dimensions, namely spherical, cylindrical and planar. They used the solution for Dirac delta source, and utilized convolution to reach the solution for finite pulse duration. Diebold et al. [47] formulated short pulse excitation of fluid samples and indicated the photoacoustic pressure wave as the spatial distribution of heat.

Inkov et al. [48] studied 1D acoustic problem of thermo-optical sound excitation in turbid medium. They considered photoacoustic effect in linear regime. They solved the photoacoustic wave equation utilizing the integral of the distribution of heat sources of an absorbing particle in a liquid. They also applied boundary conditions for the solution.

Kozhushko et al. [49] presented a theory of the transient photoacoustic behaviour. They assumed Gaussian distribution of absorbing object as optoacoustic sources and approximated the temporal profile by the Dirac delta distribution.

Diebold et al. [50] examined the photoacoustic effect generated by a spherical droplet in a fluid. They obtained acoustic wave solutions in both time domain and frequency domain considering a boundary-value problem. They also considered light pulse expressed by the Dirac delta function.

To our knowledge, photoacoustic wave equation is mostly solved for the Dirac delta shaped or Gaussian profiles since the laser used in photoacoustic phenomena is pulsed or very localized. Even though a couple of works deal with photoacoustic equation for both Gaussian radial and temporal profiles, their solutions are based on some approximations (such as far field approximation) or for some boundary conditions. Our motivation was to investigate complete analytic solution of PA wave equation for spatiotemporal Gaussian source. We present an expression for the photoacoustic signal that contains the laser parameters (pulse duration and beamwidth) and investigate the variation of the signal with respect to the corresponding parameters. We aimed to design unique laser that has adjustable parameters to experimentally investigate laser parameter dependent photoacoustics [24].

2. Method

2.1 Laser Design

Based on the physics of photoacoustics, thermal and stress confinements lead us to use a pulsed laser. In literature, three types of pulsed lasers have been used: Q-switched lasers, diode lasers and fiber lasers. The most commonly used lasers are the ones available in the market with fixed capacity in terms of pulse duration, wavelength, pulse repetition frequency and output pulse energy.

Maslov et al. built a dark field PAM system by using neodymium-doped yttrium aluminum garnet (Nd:YAG) laser with 6.5 ns pulse duration. Pulse generation was based on Q-Switching and 532 nm output was able to deliver 300 mJ energy per pulse at 10 Hz PRF [51]. In 2007, same group modified PAM system to investigate wavelength dependent fulence effect. They replaced laser with a wavelength tunable dye laser that had a range of 576-598 nm with 2 nm steps [52, 53]. In 2008, Maslov et al. developed an optical resolution photoacoustic microscopy (OR-PAM) by using Q-switched Neodymium-doped yttrium lithium fluoride (ND:YLF) laser with pulse duration of 7 ns. They reached 100 nJ pulse energy at 630 nm wavelength [11].

In 2008, Zhang et al. designed a PAI system to evaluate Fabry-Perot ultrasonic detection design [54]. They used two separate Q-switched Nd:YAG lasers. The first laser was a wavelength tunable (410-2100 nm) laser. The output of the laser had 8 ns pulse duration with 10 Hz PRF, which was measured to deliver 12-36 mJ pulse energy per pulse. The second laser they use operated at 1064 nm and had a pulse duration of 5.6 ns with 20 Hz PRF. This laser was able to deliver relatively higher pulse energy of 45 mJ.

In 2009, Jose et al. characterized Twente photoacoustic imaging system with a phantom study [55]. They used a Q-switched Nd:YAG lasers at 1064 nm, of which output had 8 ns pulse duration with 500 Hz PRF and 14 ns pulse duration with 50 Hz PRF. The laser was able to deliver 3 mJ and 2.3 mJ pulse energies respectively for corresponding operation modes.

In 2010, Shi et al. used a microchip controlled Q-switched neodymium-doped, chromium-doped yttrium aluminum garnet (Nd:Cr:YAG) laser and a passively Q-switched fiber laser [56]. Microchip laser output had 0.6 ns pulse duration and 7.4 kHz PRF at 1064 nm. Pulse energy of 1064 nm output was 1.84 μJ. The output of the laser was passed through a potassium titanyl phosphate (KTP) crystal for frequency doubling. Resultant pulses dropped to 0.21 μJ pulse energy at 532 nm. Fiber laser, on the other hand, had much longer pulse duration of 250 ns and much fast repetition rate of 100 kHz. It delivered 13 μJ pulse energy at 1075 nm wavelength. After frequency doubling, the pulse energy of the laser attenuated to 0.06 μJ at 537 nm. Although, fiber laser was approximately 10 times faster than the microchip controlled Q-switched laser, it had nearly five times less pulse energy. There was an intrinsic trade off between pulse energy and pulse repetition rate. See Section. 1.1.1.3 for pulse energy and PRF relation. In 2011, same group reached 600 kHz PRF using diode-pumped nanosecond-pulsed ytterbium-doped fiber laser emitting light at 532 nm [57].

Also in 2010, Liu et al. experimented a novel method in terms of pulse duration [58]. Rather using single nanosecond pulse, they used a sequence of picoseconds pulses and proved that sequence of pulses provide better signal to noise ratio (SNR). The laser pulse duration was 6 ps and the duration of group of pulses did not exceed 1 ns. The sequence repetition frequency was 875 kHz and each sequence had 11 nJ average pulse energy at 1064 nm.

In 2011, Allen et al. used Q-switched Nd:YAG pumped fiber laser that delivered average power of 20 W at 1064 nm [43]. The pulse duration had a range of 15 to 220 ns and PRF had a range of 10 Hz to 390 kHz. They intended to use such a high power laser for tomographic applications.

In 2012, Yeh et al. employed a solid state laser and a wavelength-tunable laser for blood pulse wave measurements. The ear of a mouse was illuminated by the wavelength tunable laser at two different wavelength of 532 and 563 nm. Absorption spectra of oxygenated hemoglobin and deoxygenated hemoglobin are utilized in order to distinguish arteries and veins [59, 60]. The laser system they used was named as second generation OR-PAM and described primarily by Hue et al. in 2011 [61].

In 2013, Zeng et al. used an aluminium gallium arsenide (AlGaAs) laser diode which provided peak output power of 140 W at peak forward current of 30 A [62]. They drove laser diode with a pulsed current driver and obtained 100 ns pulses at 800 Hz. The 65% of the pulse energy of the laser was attenuated in the lens system and 4.9 μJ pulse energy was delivered to phantom at 905 nm.

Here in this study, we use a specially designed and custom-built laser. The laser is fully integrated all-fiber mode-locked laser with adjustable parameters. As seen in Figure 2.1, fundamental component of the laser is specially designed oscillator stage, which generates pulses of 1 - 3 ns with a very high pulse repetition frequency (PRF) of 3.1 MHz. After oscillator, we have a PRF adjustment stage, which digitally controls PRF between 50 kHz and 3.1 MHz. For compensation of power loss at AOM, we utilized two pre-amplifiers at PRF adjustment stage. Then, we have a high power amplifier at the output stage to reach sufficient average power for PA generation. Finally, we have photonic crystal fiber (PCF) at the output stage in order to obtain supercontinuum at the output. The picture of laser is shown in Figure 2.2.

2.1.1 Oscillator

Oscillator is the first stage of the laser, where pulse shaping and mode-locking occurs. Mode-locked lasers require complicated management of nonlinear effects and accurate handling of pulse stretchers and compressors. The mechanisms beyond mode-locking tremendously depend on interaction of Kerr nonlinearity, dispersion, and gain [63].

Initial fiber-coupled single-mode (SM) 980 nm diode laser delivering a maximum

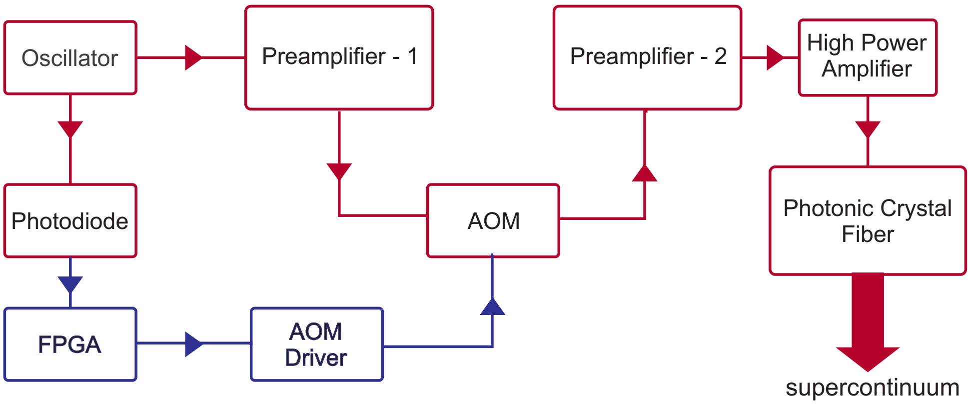

Figure 2.1 Simplified block diagram of the fully integrated all-fiber mode-locked laser. AOM: Acousto-optic modulator, FPGA: Field programmable gate array.

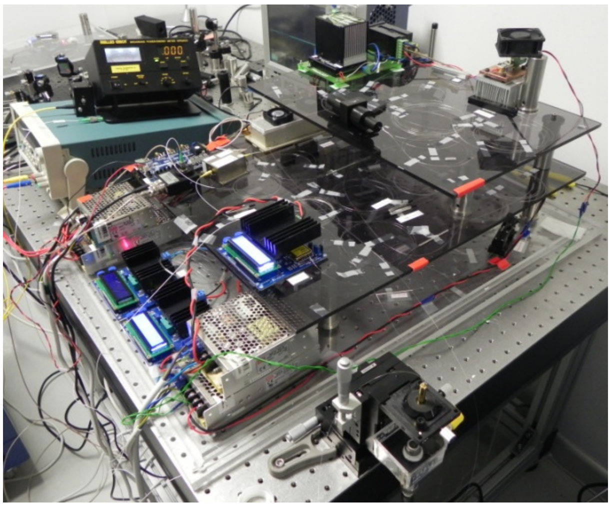

Figure 2.2 A picture of the fully integrated all-fiber mode-locked laser.

power of 650 mW is followed by a 0.7 m long Yb-doped gain fiber. Pump-protection filter rejects unwanted backward propagating light within the fiber to prevent laser diode to break down. Output of gain fiber is separated by a 70 % coupler and connected to a 8 nm bandpass filter. Although bandpass filter is not obligatory, it improves stability by filtering out pump light and adjusting central wavelength. In order to guarantee unidirectional operation, an in-line isolator is added to the circuit. Using an output coupler of 10% of isolator a reference clock output is fed to the next stage. Then two polarization controllers added in order to utilize nonlinear effects and to assist mode-lock operation. A 50 m long HI-1060 single mode fiber is used for Sagnac loop, which also consists of a 2x2 40% coupler for non linear optical loop mirror (NOLM) [64]. The fundamental repetition rate of the cavity is 3.1 MHz. 10% of the oscillator output seeds the amplification stage with oscillations of 24 mW power and 8 nJ energy. Figure 2.3 shows the schematics of the oscillator setup. Oscillator design is the most crucial part of a fiber laser. The specifications of the laser, namely pulse duration and pulse repetition frequency, are determined by the lengths of fibers and polarization controllers. The unique design of oscillator allows us to adjust mentioned parameters.

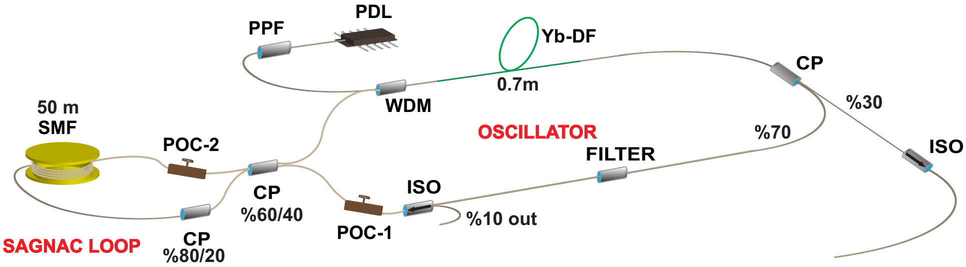

Figure 2.3 Schematic of the oscillator stage of the laser. PDL: Pump diode laser, WDM: Wavelenght-division multiplexer, Yb-DF: Yttirbium-doped fiber, CP: Coupler, ISO: Isolator, POC: Polarization controller, SMF: Single mode fiber.

2.1.2 PRF Adjustment

The fundamental frequency of the cavity is extremely fast for PA applications. Considering propagation speed of the acoustic waves in biological tissues (~ 1.5 mm/μsec), consecutive pulses hit the tissue before acoustic wave travels out of the focal spot of the laser. Due to this temporal resolution phenomena, we added PRF adjustment to the laser. The secondary reason for lower PRF requirement is the need for controlling energy per pulse value. At final amplification stage, the power of the pump source, and dependently the output average power is constant. The relation between PRF and average power can be formulated as [31]

$$P_{AVG} = E_{pp} f_{pr} \tag{2.1}$$

where P_{AVG} is the average power, E_{pp} is the energy per-pulse, and f_{pr} is pulse repetition frequency. Obviously seen in Eq. 2.1, for a constant average power, pulse repetition rate and energy per-pulse are inversely proportional. Therefore, our laser delivers more peak power at 50 kHz.

The 10% reference output of the oscillator is converted to electrical pulses with a photodetector (EOT 3500F) and fed to a field programmable gate array (FPGA) as a clock signal. Based on the clock signal, a new pulse train with desired frequency is generated. This new pulse train is used to enable signal of acousto-optical modulator (AOM) driver. The AOM filters out certain portion of the optical pulses and adjusts PRF of the output. In Figure 2.4, the plot of optical pulse train fed to the FPGA and output of FPGA connected to AOM is displayed. FPGA creates square pulse windows to selectively enable AOM driver. Note that, dealing with very fast pulses requires extra care for delay handling. Thus, the lengths of electrical transmission lines and optical fibers becomes important to achieve overlap on optical and electrical pulses.

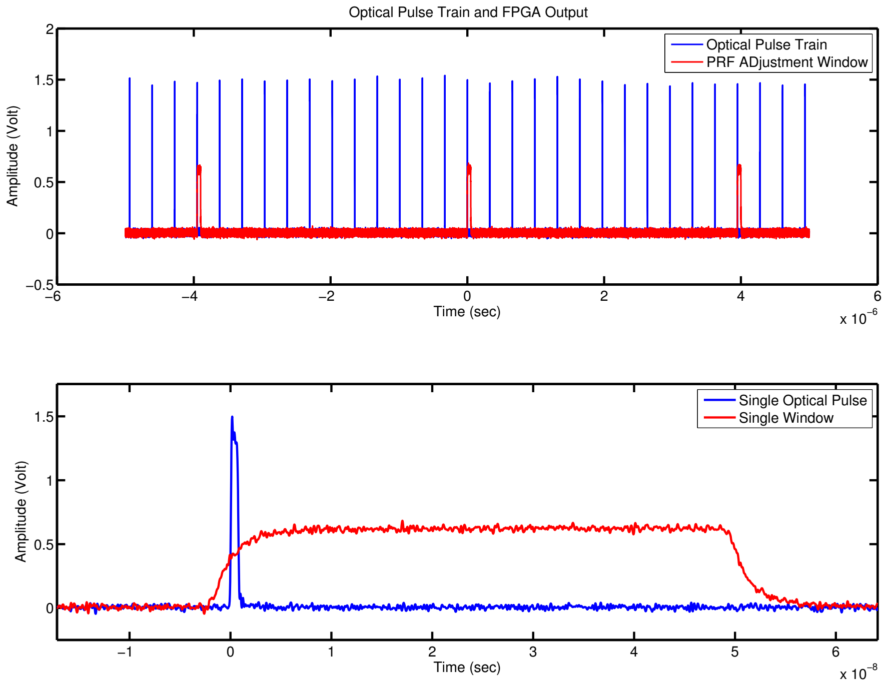

Figure 2.4 PRF adjustment method by filtering undesired pulses with AOM.

Since, there occurs a power drop at AOM, two preamplifier stages are added to the system to compansete power loss. Figure 2.5 shows the schematic of two preamplifier stages, AOM and FPGA that used in the laser.

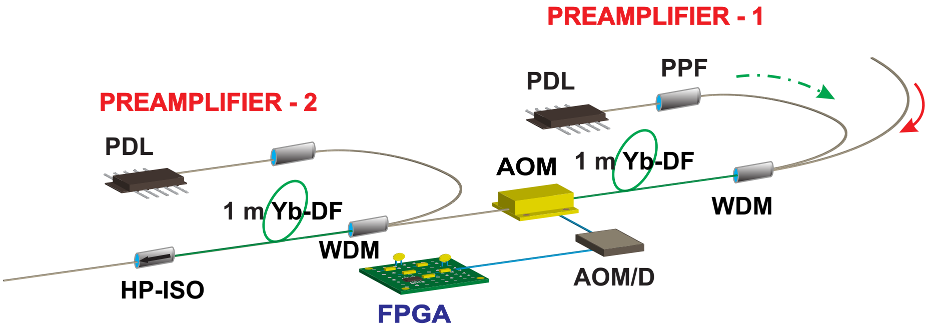

Figure 2.5 Schematic of preamplifers and PRF adjustment stage. PDL: Pump diode laser, PPF pump protection filter, Yb-DF: Yttirbium-doped fiber, WDM: Wavelength-division multiplexer, AOM: Acousto-optical modulator, AOM/D: Acousto-optical modulator driver, FPGA: field programmable gate arrays, HP-ISO: High power isolator.

2.1.3 High Power Amplifier

The pulse energy and implicitly the average power is important to generate detectable PA waves. Hence, we need a final amplifier stage to compensate losses and increase the output power to a sufficient level. We use a 980 nm 25 W (Oclaro BMU25-980-01/02-R) laser diode as a pump source and a 2.8 m long double-clad Yb:doped fiber for gain medium as seen in Figure 2.6.

The average power at the output of gain fiber increases linearly with current supplied to the driver of high power pump diode laser until a certain current. After a threshold current, temperature stability of pump source is disturbed and linearity diminishes.

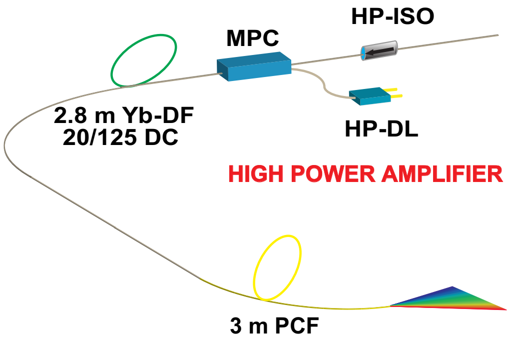

Figure 2.6 Final amplifier stage pumped by a high power laser diode. HP-DL: High power diode laser, HP-ISO: High Power Isolator, MPC: Multiple Pump Combiner, PCF: Photonic Crystal Fiber.

2.1.4 Photonic Crystal Fiber and Supercontinuum Generation

A photonic crystal fiber (PCF) is a microstructured optical fiber which guides the light in its tiny and closely spaced air holes rather than a glass composition. PCFs are manufactured by extrusion method and generally made of soft glass or polymers [65]. The variety of hole arrangements lead various features and applications of PCFs. All unique PCF can be considered as speciality fiber [31]. Photonic crystal fibers are recently spotlighted due to their nonlinear waveguide nature. The variety of structures and nonlinearity of PCFs, makes them a milestone in nonlinear optics.

Generation of new spectral components is inherent nature of nonlinear optics. Spectral broadening has been known since early 1960s [66]. When a monochromatic light undergoes a nonlinearity through its waveguide, a spectral broadening yields a continuous broad spectrum. Supercontinuum generation is first reported by Alfano and Shapiro in 1970 in bulk glass material [67]. In 2002, Harbold et al. demonstrated continuum generation in tapered fiber [68].

In this study, the PCF of 3.5 meter length is spliced to a double clad Yb-doped fiber of the final amplifier for supercontinuum generation. Since the fusion splicing of gain fiber and PCF is a very hard and ineffective, we use LMA and SM fibers in between. The power delivery between wide core fiber to photonic crystal fiber is around

35%; thus, the output power is 600 mW corresponding to 6 μJ pulse energy. Due to its air silica honeycomb-like microstructure, nonlinear optical propagation is enhanced in the PCF [58]. The zero dispersion wavelength of the PCF is 1040 nm. Spectral width of supercontinuum is 500 nm starting from 600 nm and ending at 1100 nm. Figure 2.7 shows supercontinuum spectrum.

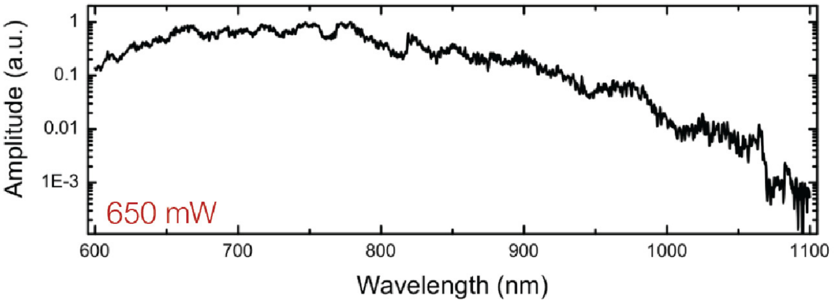

Figure 2.7 Normalized spectrum of supercontinuum at the PCF output.

2.2 Ultrasound Hardware

2.2.1 Transducer Characterization

For the ultrasonic hardware, we use focused immersion ultrasonic transducers of Olympus Panametrics, with central frequency of 3.5 MHz, 10 MHz and 50 MHz. In order to maximize the amplitude of received pressure waves, we need to characterize transducers.

We did focal distance characterization of pulse echo signals. We recorded pulse echo signals of 10 MHz data in 55.88 mm distance range in 40 step. Each rotation of linear stage (Thorlabs - LT3/M) corresponding to a 1.397 mm shift in the position of the tip of the transducer. Since we are working in pulse-echo mode, propagation distance of ultrasonic waves between the transducer and the first boundary changes twice of the stage shift. Speed of sound in water is considered as 1.473 mm/μsec [69] and time delay between two reflected waves are measured as 1.897 μsec as seen in 2.8

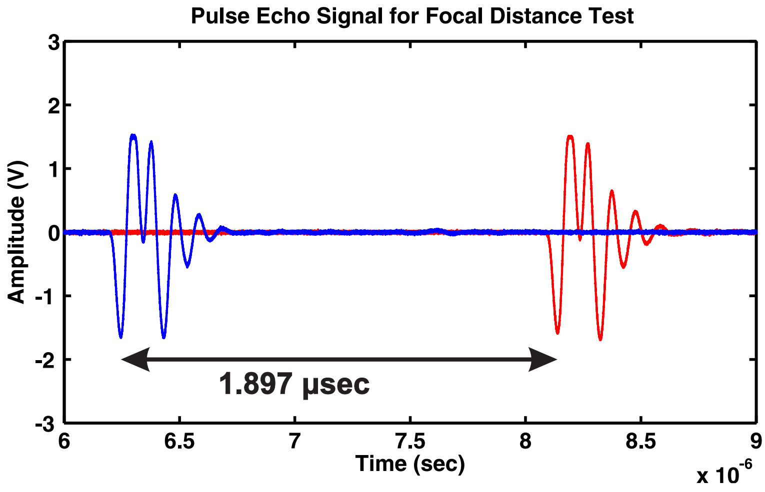

Figure 2.8 Time shift of two echo signal due to linear stage movement.

Shift in the position of the tip of the transducer is calculated as,

$$d = v_us \times t_delay = 2.794mm \tag{2.2}$$

which is exactly equal to the twice of position shift. Considering 40 different data, we observe perfect linearity in ultrasonic distance measurements.

Despite the linear increase in distance, amplitude of ultrasound signal stays constant. Static pulse amplitude reveals that the gain of received signals does not depend on the distance from the transducer. In order to minimize attenuation in water, we minimized the distance of transducer from the sample.

2.3 Data Acquisition and Signal Processing

Data acquisition is done by a PCIe data acquisition (DAQ) card manufactured by GageRazor. DAQ card has 14 bit resolution with 200 Msps sampling rate and 125 MHz bandwidth. Optimal ultrasound frequency is below the 125 MHz for our application. Thus, DAQ system fulfils the requirement for photoacoustic microscopy.

A MATLAB environment software development kit (SDK) is available for the DAQ card, which enables us to record PA data in video rate. Signal is 100 sweep averaged and filtered out with cascaded lowpass and highpass filters. Filtering details are mentioned in Section 2.3.1.

Alternatively, we use a 4 GHz oscilloscope (LeCroy® WaveMaster 806ZiA) in order to record scan data. In this method, real time data acquisition is not utilized. Data is stored in the hard drive of the oscilloscope and transferred to the computer.

2.3.1 MATLAB® Graphical User Interface

We designed a graphical user interface (GUI) is in MATLAB® to adjust pass-band cut-off frequencies of the filters. GUI has the capability of down sampling and visualize the resultant signal immediately. The filtering part is consisted of a low pass filter, a high pass filter and a notch filter. Figure 2.9 shows a capture of GUI window. We coded the MATLAB® GUI to employ it in pre-experiment step. Before making the experiment mentioned in Section 2.3.3, we acquired sample data from single horse hair in order to decide filter specifications and choose appropriate transducer.

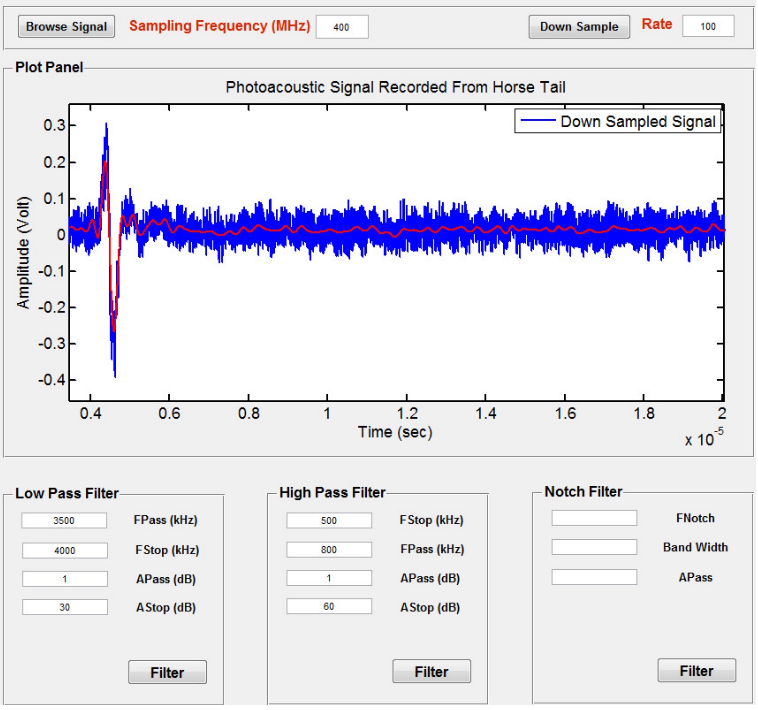

Sampling Frequency (MHz) 400
Rate 100

Low Pass Filter
3500 FPass (kHz)
4000 FStop (kHz)
1 APass (dB)
30 AStop (dB)

High Pass Filter
500 FStop (kHz)
800 FPass (kHz)
1 APass (dB)
60 AStop (dB)

Notch Filter
FNotch
Band Width
APass

Figure 2.9 MATLAB GUI designed to tune digital filter parameters for the set up used in photoacoustic microscopy.

2.3.2 B-Mode Image Formation

Image formation in photoacoustic microscopy do not require a complicated reconstruction algorithm. We assumed that acoustic signals do not scatter and do not attenuated significantly. Hence, we considered a straightforward algorithm to obtain Brightness mode (B-mode) images of photoacoustic signals.

B-mode imaging is the most widely used mode in medical ultrasonic imaging. A B-mode image represents anatomical organ and tissue boundaries of a cross sectional region. Instrument is operated at pulse-echo mode, and echo signals are the source of B-mode images. The 2D information required for B-mode imaging is obtained by scanning by phased array transducers. As seen in Figure 2.10, each line represents the direction of scanning and the amplitude line (A-line) recorded by corresponding transducer element.

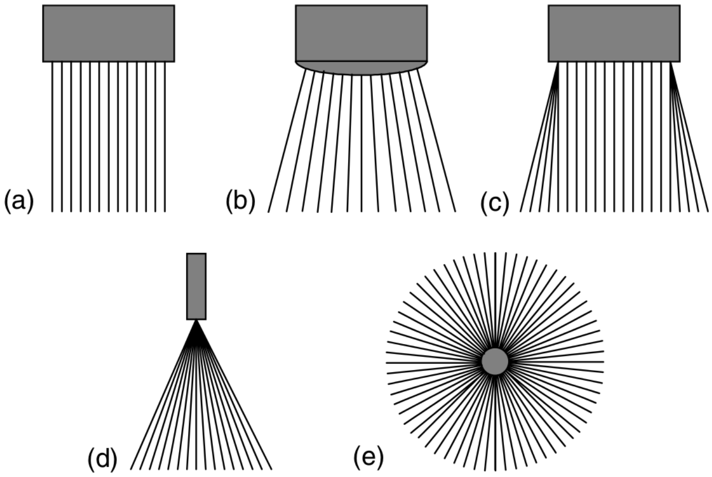

Figure 2.10 Scan line arrangements for commonly used medical ultrasound.(a) linear, (b) curvilinear,(c) trapezoidal, (d) sector and (e) radial [70].

Raw echo signals are amplified and digitized. Then, time gain compensation is utilized in order to compensate the attenuation in deeper tissue. In B-mode imaging, only the amplitudes of received echoes are the matter of interest. Therefore, envelope of signal is detected with Hilbert transform. And resultant signal is transformed into a 2D matrix, of which amplitudes represent gray scale level of corresponding pixel.

Presently, more complicated algorithms may be used to enhance the imaging performance of ultrasound imaging. However, we will not further explain the details of B-mode imaging. We use the most general and basic method of B-mode imaging in photoacoustic microscopy. Figure 2.11 represents image formation procedure used in photoacoustic B-mode images.

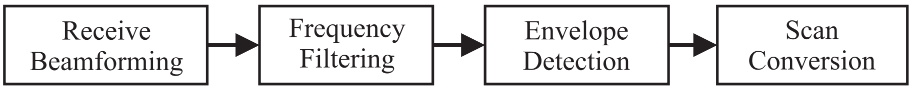

Figure 2.11 Image formation algorithm of B-mode imaging.

2.3.3 Phantom Experiments

We constructed different phantoms using horse hair. For all phantoms, we employed a $30 \times 50 \times 80$ mm aluminium block with 25 mm cylindrical hole in its center to fix hairs inside the immersion tank. We made the first phantom by fixing a single hair on the aluminium block in such a way that it coincides with the diameter of that cylindrical hole. For the second phantom, we designed a 2x2 grid phantom using four horse hair with average thickness of 280 μm. Figure 2.12 shows the picture of the hair grid phantom and the image of the phantom under the light microscope. Taking data on the single hair gives information about PSF of the imaging system. For the images and the results see Chapter 3. We preferred horse hair due to its thickness and its intrinsic nature of absorption.

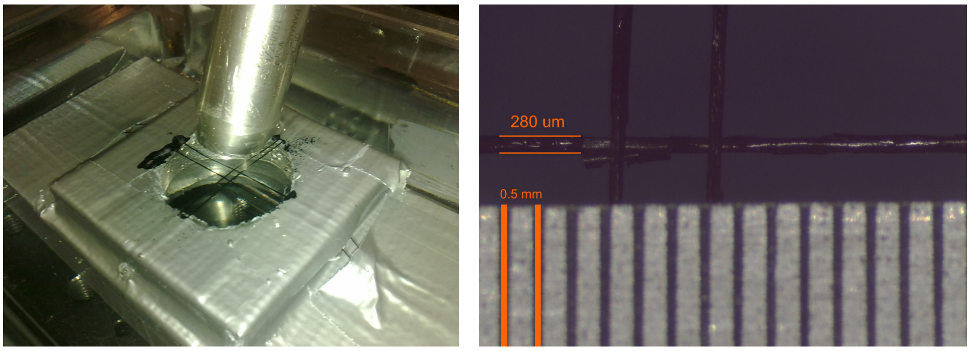

Figure 2.12 A picture of grid phantom made of horse hair and its image under light microscope.

3. Results

3.1 Phantom Experiments

The experiments conducted with horse hair phantoms aimed to characterize PSF of our microscopy system.

In Figure 3.1, a B-scan image in the vertical axis represents the intersection of the two horse hair with scanning axis. The two horse hairs are clearly observable and the amplitudes of PA waves follow a Gaussian distribution. The diagonal shape of the PSFs of the horse hairs is an artefact of scanning method in the very first setup. Instead of scanning the laser light we move sample via linear stage. Thus, the distance that PA waves propagates changes at each step, and image seems as if signals are coming from a deeper region in the sample. PSF of the PAM system is large for microscopic purposes.

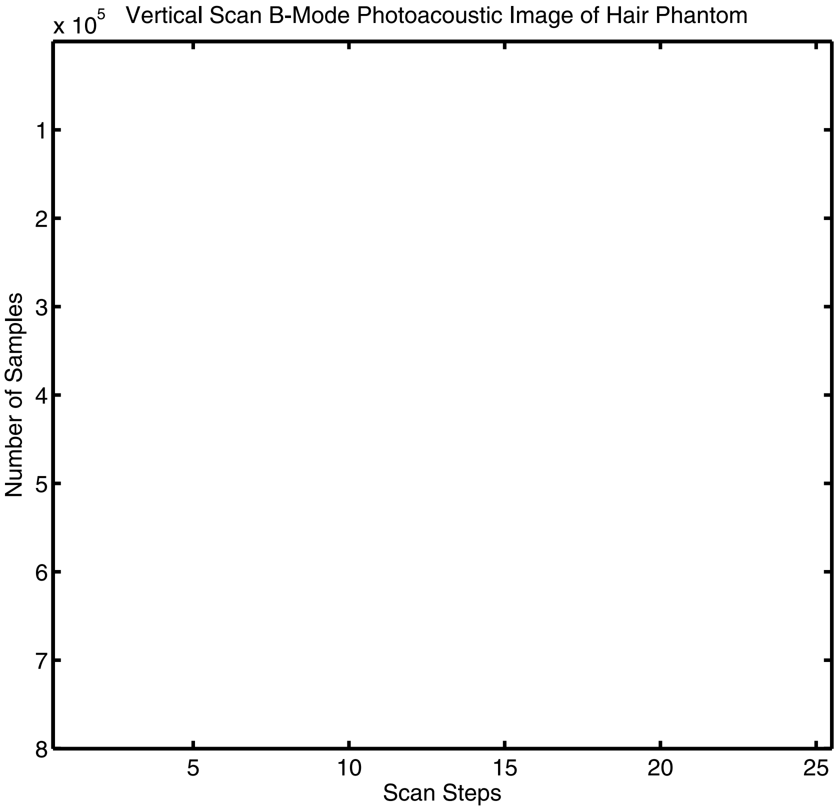

Figure 3.1 Vertical B-scan image of grid phantom recorded at $\sim$ 3 mm focal spot size and scanned with 350 μm linear stage steps.

However, the results are reasonable due to large focal spot size. Our beamwidth is comparably larger than the target size (280 μm for horse hair) and laser pulses hit the target even the absorber is out of the region of interest.

In Figure 3.2, a B-scan image of single hair phantom represents a better axial and lateral resolution. For this image, we employ a of a narrower beamwidth. Hence, the laser pulses do not hit the hair when is not in the region of interest. Figure 3.3 shows a more detailed scan of the one of the hairs in grid phantom. With this experiment, width of PSF of our PAM is calculated to be around 500 μm.

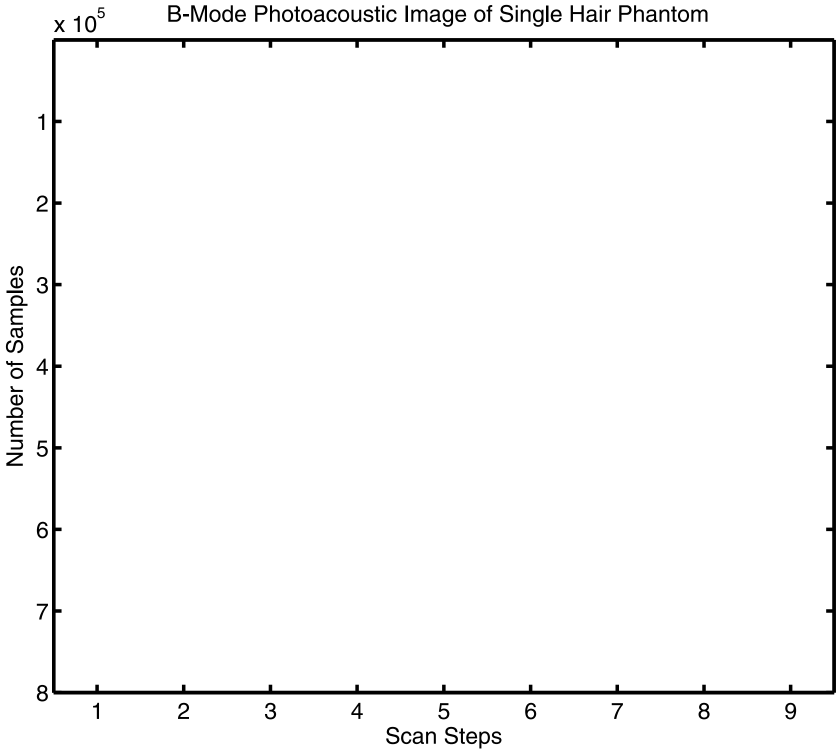

Figure 3.2 B-scan image of single hair phantom recorded at sub-millimeter focal spot size and scanned with 170 μm linear stage steps.

3.2 Photoacoustic Waves at Different Pulse Repetition Frequency

In order to investigate PRF affect over PA wave amplitude we acquired three set of data. At each set, current of high power diode driver is swept from 1 A to 4 A

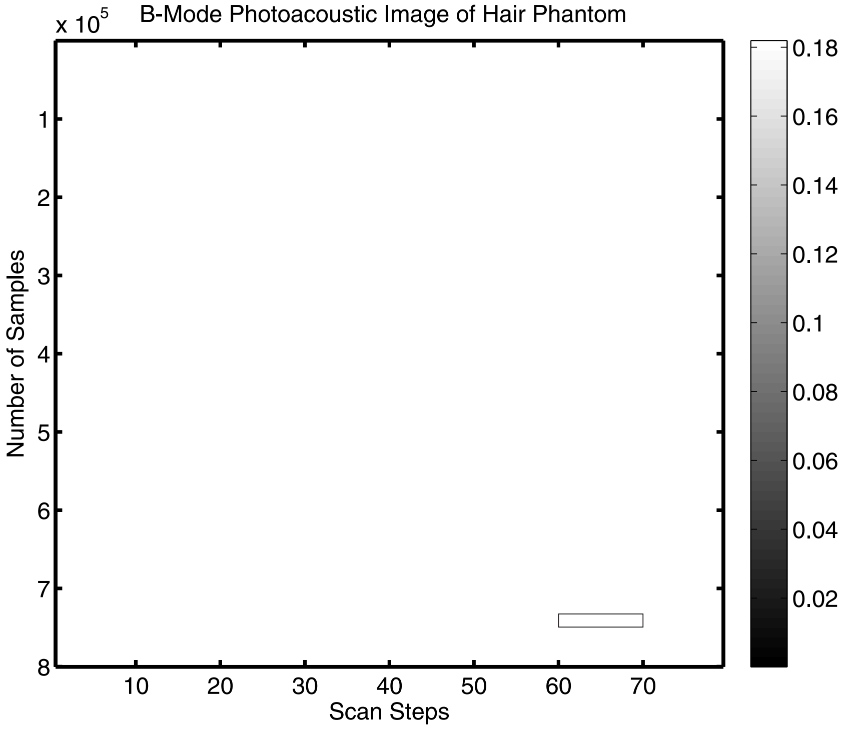

Figure 3.3 B-scan image one hair in the grid phantom recorded at sub-millimeter focal spot size and scanned with 15 μm linear stage steps.

with 500 mA steps. The current range corresponds an output power range of 50-1100 mW after double-clad Yb-DF. In Figure 3.4, a PA signal is shown as N-shaped pressure wave. The second positive peak after initial peak is the echo of the generated PA wave travelling in forward direction.

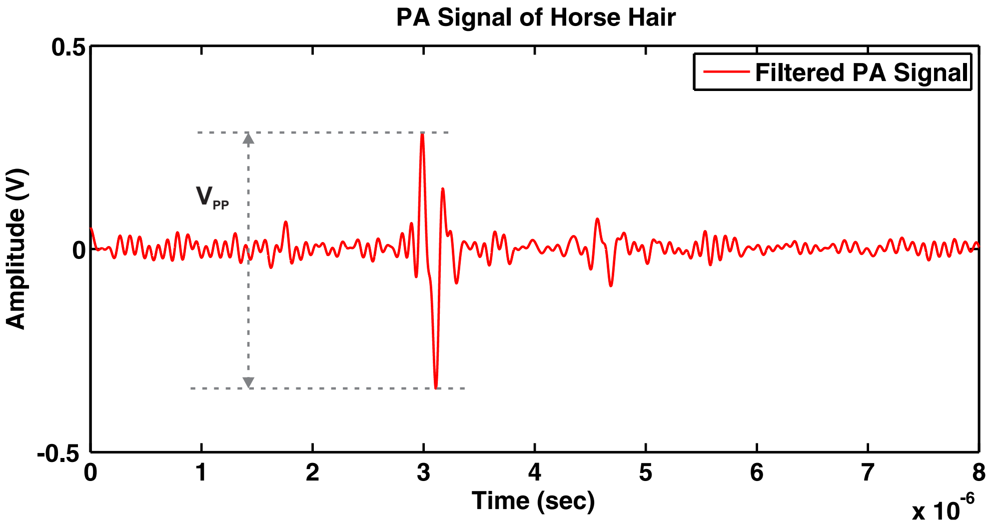

Figure 3.4 A sample PA signal generated at 50 kHz.

For the amplitude comparison, we consider peak to peak voltage value of the response of the transducer. As seen in Figure 3.5, amplitude of the pressure wave linearly changes with average power of the laser. Moreover, the slope of each line is proportionally changes with PRF of the laser.

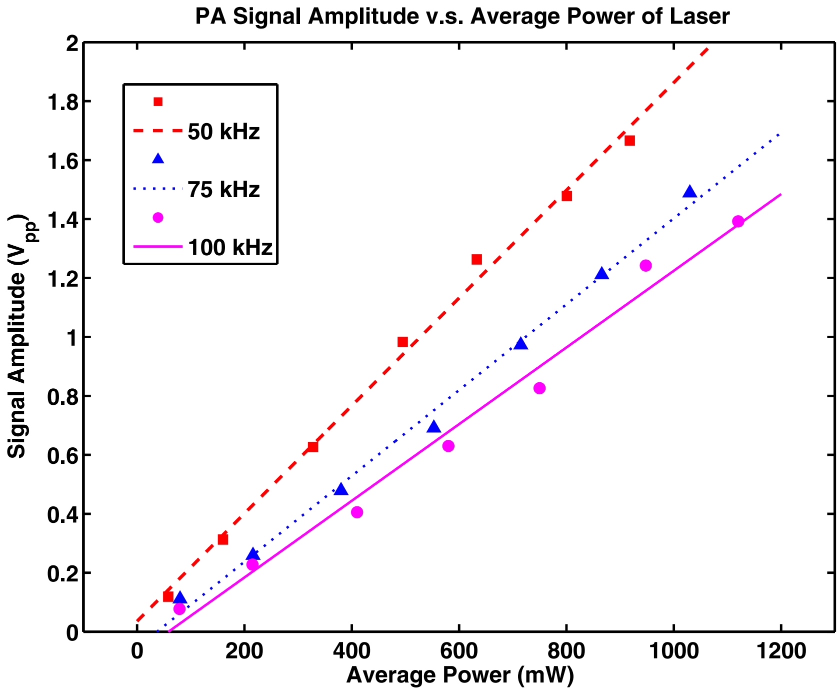

Figure 3.5 PA wave amplitudes for different pulse energies at different pulse repetition frequency.

4. Discussion

Photoacoustic microscopy is advantageous to other microscopy methods used in life sciences in terms of few aspects. PAM is capable of imaging live cells *in vivo*. Moreover, the chromophores that create contrast in PAM are inherent in biological components. It does not require fluorescence proteins. For example in cancer research, it is possible to image micro-vascularization in vivo via PAM even for deeper regions than 3 mm. This unique opportunity accelerates animal studies in cancer research.

PAM image quantifiers such as x-y resolution (lateral) and z resolution (axial) strongly depends on the properties of laser and ultrasound hardware specifications.

For the ultrasonic hardware, we used 10 MHz transducer with a pre-amplifier and a pulser receiver with a total gain of 79 dB. Ultrasonic detection part of PAM is quite trivial and straightforward. The only variable is the ultrasound frequency. Although 10 MHz transducer receives signals, we are planning to use 50 MHz transducer for biological samples. Since the size of absorbers in samples determines the generated frequency of ultrasound waves, tissue level vessels and capillaries requires such a high frequency transducers. Along with transducer, amplifiers and analog filters are needed to be replaced with suitable ones.

The laser excitation requires careful handling of all parameters based on application. Imaging depth of the microscopy system is inversely proportional with lateral resolution. For example, pulse duration of the laser should be in the order of nanoseconds in order to generate PA waves efficiently. Violation of thermal and stress confinements cause heat diffusion to become active degrades the effect of sudden thermal expansion. Hence, the amplitude of the detected waves decays with increasing pulse duration. However, another question arises at this point: Is the change of the amplitude of PA wave significant for comparable pulse duration, which secure thermal and stress confinements. Our custom-made laser has 1-3 ns adjustable pulse duration. Our next study will focus on the PA wave analysis depending on different pulse duration in the adjustable range.

One of the crucial features of lasers, the beamwidth, is highly correlated with resolution and depth of imaging of PAM system. If the laser light is tightly focused this improves lateral resolution. However, photon flux is also increases and creates a concern about pulse energy of the laser. If absorption of the surrounding tissue is not negligible, we should decrease the amplification of optical pulses not to damage the surface of the target tissue. Less pulse energy yields much attenuation on the path of light and decreases the penetration depth of light. Focal spot size of the laser also determines the frequency of generated PA wave. Smaller focal spot results in a higher frequency of ultrasound, which also increases ultrasonic attenuation and decreases depth of imaging.

In our PAM system, the size of the focal spot is determined by lens system and it is possible to expand the beam replacing lens system. Our results represent the relation between beamwidth and resolution. As the beamwidth increases, the axial and lateral resolutions decreases accordingly.

Pulse repetition frequency of the laser is an important parameter to achieve sufficient imaging speed for clinical purposes. Our unique design allows us to adjust PRF between 50 kHz and 3.1 MHz by using FPGA. 3.1 MHz is a sufficient frequency for video rate imaging. Although our novel fiber laser is considerably fast, we decrease the frequency of the pulses due to acoustic speed limitations. We anticipate a further decrease in PRF for biological experiments in the case that the pulse energies after spectral filtering are insufficient.

The results obtained based on PRF investigation are consistent with the theory considered photon fluence. As the average power increases for a specific repetition frequency pulse energy also increases, which yields a linear increase in the amplitude of received signal. Moreover, for the same average power, lower PRF yields a higher pulse energy. This is obviously seen in the results that 50 kHz line has a highest slope among three lines. Hence, actual linear correlation exists between initial PA pressure and fluence. If we consider PRF value and calculate pulse energy from average power, we observe that all data creates a single linear function. This conclusion perfectly matches with the theory about PRF and fluence. This means that the optical energy that is transferred to the absorbing volume determines the generated pressure.

Signal-wise investigation of laser pulse energy or PRF guides us through better SNR and less noisy images. Thus, we do not repeat B-scan images for different PRF in the scope of this thesis.

Employing the PCF at the output, we generate a continuous wavelength spectra between 600 nm and 1100 nm. The aim of using supercontinuum is to have the flexibility to adjust the wavelength via filtering. We are planning to use discrete filters with various central wavelengths. Hereby, we are able to excite different chromophores in biological samples. Instead of using discrete filters, an acousto-optic filtering is a feasible method to filter spectrum continuously. In the scope of this dissertation, we did not utilize supercontinuum. We measured PA data excited by the 1064 nm output before PCF. Here in this study, we only excited a single target, that is horse hairs in our phantom. Our ultimate goal is expanding our way to different probes by adjusting wavelength and obtain spectroscopic images.

In this thesis, the novelty is the fully adjustable, supercontinuous, mode-locked fiber laser. By the help of this custom-made laser, we have the unique opportunity to experimentally validate laser parameter dependencies of PA waves.

APPENDIX A. Solution of Photoacoustic Wave Equation for a Dirac Delta Source

Once generated, the pressure propagation can be modeled as wave propagation and described by a wave equation. The source term in the wave equation H is highly correlated with light parameters and medium properties. Obtaining a general analytic solution based on beam intensity distribution and absorbing volume geometry becomes compelling. However, point source assumption leads quite accurate results in practice. The solution to the photoacoustic wave equation, specified in Eq. A.1, can be obtained by using the Green's function approach [23]. Wang solved the photoacoustic equation by treating the source term as a Dirac delta function in time domain [9, 18]

$$(\nabla^2 - \frac{1}{v_s^2}\frac{\partial^2}{\partial t^2})p(\boldsymbol{r},t) = -\frac{\beta}{\kappa v_s^2}\frac{\partial^2 T(\boldsymbol{r},t)}{\partial t^2} \tag{A.1}$$

where v_s is acoustic propagation speed, $p(\boldsymbol{r},t)$ is pressure wave in time t and space coordinate r, β is the thermal coefficient of volume expansion, κ is the isothermal compressibility, and $T(\boldsymbol{r},t)$ is temperature at position $\boldsymbol{r}$ and time t [18]. Replacing $p(\boldsymbol{r},t)$ with Green's function and source term with Dirac delta function

$$(\nabla^2 - \frac{1}{v_s^2}\frac{\partial^2}{\partial t^2})G(\boldsymbol{r},t;\boldsymbol{r},t') = -\delta(\boldsymbol{r}-\boldsymbol{r'})\delta(t-t') \tag{A.2}$$

the Green's function in Eq. A.2 for unbounded space is given by

$$G(\boldsymbol{r},t;\boldsymbol{r},t') = -\frac{1}{4\pi \mid \boldsymbol{r}-\boldsymbol{r'} \mid}\delta(t-t'-\frac{\mid \boldsymbol{r}-\boldsymbol{r'} \mid}{v_s}) \tag{A.3}$$

and the following integral gives solution to photoacoustic wave equation

$$p(r,t) = \int_{-\infty}^{t^+} dt' \int dr' G(\boldsymbol{r},t;\boldsymbol{r},t')\frac{\beta}{\kappa v_s^2}\frac{\partial^2 T(\boldsymbol{r'},t')}{\partial t'^2}. \tag{A.4}$$

Substituting G in Eq. A.3 into Eq. A.4 and simplifying the expression by replacing Dirac delta integral $\int_{-\infty}^{t^+}\delta(-t'+t-\frac{|\boldsymbol{r}-\boldsymbol{r'}|}{v_s})dt' = 1$ for $t' = t-\frac{|\boldsymbol{r}-\boldsymbol{r'}|}{v_s}$ we get

$$p(r,t) = \frac{\beta}{4\pi\kappa v_s^2}\int dr' \frac{1}{\mid \boldsymbol{r}-\boldsymbol{r'} \mid}\frac{\partial^2 T(\boldsymbol{r'},t')}{\partial t'^2} \tag{A.5}$$

Based on short pulse assumption we can transfer the source term from temperature distribution to heating function as follows

$$\rho C_V \frac{\partial T(\boldsymbol{r},t)}{\partial t} = H(\boldsymbol{r},t) \tag{A.6}$$

and we get

$$p(r,t) = \frac{\beta}{4\pi C_P} \int dr' \frac{1}{\mid \boldsymbol{r}-\boldsymbol{r'} \mid} \frac{\partial H(\boldsymbol{r'},t')}{\partial t'}. \tag{A.7}$$

Taking derivative operator outside of the integral we get

$$p(r,t) = \frac{\beta}{4\pi C_P} \frac{\partial}{\partial t} \int dr' \frac{1}{\mid \boldsymbol{r}-\boldsymbol{r'} \mid} H(\boldsymbol{r'}, t - \frac{\mid \boldsymbol{r}-\boldsymbol{r'} \mid}{v_s}). \tag{A.8}$$

Note that we can decompose $H(\boldsymbol{r'},t')$ into space and time components as $H(\boldsymbol{r'},t) = H_s(\boldsymbol{r'})H_t(t')$ and substitute its equivalent into Eq. A.8 we attain

$$p(r,t) = \frac{\beta}{4\pi C_P} \frac{\partial}{\partial t} \int dr' \frac{H_s(\boldsymbol{r'})}{\mid \boldsymbol{r}-\boldsymbol{r'} \mid} H_t(t - \frac{\mid \boldsymbol{r}-\boldsymbol{r'} \mid}{v_s}). \tag{A.9}$$

The temporal component of heating function has a Dirac delta distribution based on short pulse assumption. However, spatial component of heating function is not that obvious. Starting from thermoelastic expansion, we can estimate spatial component. The pressure rise just after the laser excitation can be expressed in terms of the optical absorption coefficient and the optical fluence considering the following fractional volume expansion [18]

$$\frac{dV}{V} = -\kappa p + \beta T \tag{A.10}$$

where T is the increase in temperature.

The stress confinement condition leads us to conclude zero volume change initially. Left hand side of Eq. A.10 becomes zero and the initial pressure rise just after the pulse can be written as [18, 71]

$$p_0(r) = \frac{\beta T(r)}{\kappa} \tag{A.11}$$

$$\kappa = \frac{C_P}{\rho {v_s}^2 C_P} \tag{A.12}$$

Assume that all the optical energy converted to heat we can write,

$$T(r) = \frac{A_e(r)}{\rho C_V} \tag{A.13}$$

which yields

$$p_0(r) = \frac{\beta}{\kappa \rho C_V} A_e(r) \tag{A.14}$$

where $A_e(r)$ denotes for the specific optical absorption. It can be expressed as $A_e(r) = \mu_a(r)F(r)$. All the electromagnetic energy is converted to heat, than the spatial component of the heating function $H_s(\boldsymbol{r})$ can be equivalent to optical absorbed energy and considered as proportional to initial pressure. Which yields

$$H_s(\boldsymbol{r}) = p_0(\boldsymbol{r}) \frac{\kappa \rho C_V}{\beta} \tag{A.15}$$

Taking delta excitation $H_t(t') = \delta(t - \frac{|\boldsymbol{r}-\boldsymbol{r'}|}{v_s})$ and substituting Eq. A.15 into Eq. A.9 we get

$$p(r,t) = \frac{1}{4\pi v_s^2} \frac{\partial}{\partial t} \int dr' \frac{p_0(\boldsymbol{r})}{\mid \boldsymbol{r} - \boldsymbol{r'} \mid} \delta(t - \frac{\mid \boldsymbol{r} - \boldsymbol{r'} \mid}{v_s}) \tag{A.16}$$

For a spherical object with radius R the reference geometry for source and observer is seen in Figure A.1. For spherical geometry $p(r,t)$ can be represented by

$$p(r,t) = p_0[\theta(R - v_s t - r) + \frac{r - v_s t}{2r} \theta(r - \mid R - v_s t \mid) \theta(R + v_s t - r)]. \tag{A.17}$$

Since, initial pressure rise is valid for inside the sphere, we can approxiamte p_0 as

$$p_0(r) = \theta(r)\theta(-r + R). \tag{A.18}$$

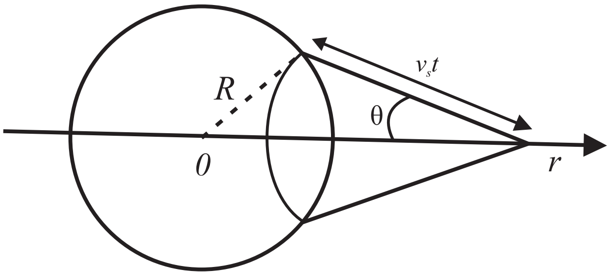

Figure A.1 Source and observer geometry for spherically absorbing object [18].

Final expression for pressure distribution at a point r outside a spherical object with radius R is found as

$$p(r,t) = \frac{r + v_s t}{2r} p_0(r + v_s t) + \frac{r + v_s t}{2r} [p_0(r - v_s t) + p_0(-r + v_s t)] \tag{A.19}$$

The first term on the right hand side represents a converging spherical wave and rest of the terms stand for diverging waves.

Upon delta heating an initial p_0 is generated. This initial pressure rise triggers two seperate spherical waves travelling in opposite direction. One travels outward and diverges, while the other one travels inward and converges towards the center of the source. When reached center, it becomes a diverging spherical rarefaction wave [18]. The bipolar, N-shape wave phenomena is accountable.

The first term on the right hand side is converging spherical wave and rest of the terms represent diverging terms [9]. Upon delta heating an initial p_0 pulse is generated. This initial pressure rise triggers two sperate spherical waves travelling in opposite directions. One travels outward and diverges and the other one travels inward and converges towards the center of the sphere. When reached to center, it becomes a diverging spherical rarefaction wave [18].

APPENDIX B. Solution of Photoacoustic Wave Equation for a Spatiotemporal Gaussian Source

In this section, we treat the radial absorption profile as Gaussian which is a more comprehensive case compared to the uniform radial profile case

$$p_0(r) = p_0 \exp(-\frac{r^2}{2\tau^2})\theta(r)\theta(-r+R) \tag{B.1}$$

where τ is the standard deviation or beamwidth of the laser. Fourier transform of $p(r,t)$ gives

$$\begin{aligned}\tilde{p}(r,\omega) &= \frac{p_0}{2\pi}\frac{1}{v_s r}\exp[-\frac{\sigma^2\omega^2}{2}] \\ &\int_0^R r' \exp(-\frac{r'^2}{2\tau^2})[\exp[i\frac{\omega}{v_s}(r-r')] - \exp[i\frac{\omega}{v_s}(r+r')]]dr'.\end{aligned} \tag{B.2}$$

The solution of the photoacoustic equation in time domain can be obtained by calculating the following integral

$$\begin{aligned}p(r,t) &= \frac{p_0}{2\sqrt{2\pi}}\frac{1}{v_s r}\int_0^R r' \exp(-\frac{r'^2}{2\tau^2})\int_{-\infty}^{\infty}\{\exp[-\frac{\sigma^2\omega^2}{2} + i\omega(\frac{r-r'}{v_s} - t)] \\ &- \exp[-\frac{\sigma^2\omega^2}{2} + i\omega(\frac{r+r'}{v_s} - t)]\}d\omega dr'.\end{aligned} \tag{B.3}$$

Substituting

$$\int_{-\infty}^{\infty}\exp[-\frac{\sigma^2\omega^2}{2} + i\omega(\frac{r \mp r'}{v_s} - t)]d\omega = \frac{\sqrt{2\pi}}{\sigma}\exp[-\frac{(\frac{r\mp r'}{v_s} - t)^2}{2\sigma^2}] \tag{B.4}$$

into Eq. B.3 leads to

$$\begin{aligned}p(r,t) = \quad & \frac{p_0}{2}\frac{1}{v_s r\sigma} \\ & \int_0^R r'\{\exp[-\frac{r'^2}{2\tau^2} - \frac{(\frac{r-r'}{v_s} - t)^2}{2\sigma^2}] - \exp[-\frac{r'^2}{2\tau^2} - \frac{(\frac{r+r'}{v_s} - t)^2}{2\sigma^2}]\}dr'\end{aligned} \tag{B.5}$$

for outside the object ($r > R$). Calculations of

$$J_{1,2} = \int_0^R r' \exp[-\frac{r'^2}{2\tau^2} - \frac{(\frac{r\mp r'}{v_s} - t)^2}{2\sigma^2}]dr' \tag{B.6}$$

integrals which are on the right hand side of Eq. B.5 yield

$$\begin{aligned}
J_1 \quad &= \int_0^R r' \exp[-\frac{r'^2}{2\tau^2} - \frac{(\frac{r-r'}{v_s} - t)^2}{2\sigma^2}]dr' \\
&= \frac{\sigma\tau^2 v_s}{2(\tau^2 + \sigma^2 v_s^2)^{3/2}} \exp[-\frac{(r - v_s t)^2}{2\sigma^2 v_s^2}] \\
&\times\{\sqrt{2\pi}\tau(r - v_s t) \exp[\frac{\tau^2(r - v_s t)^2}{2\sigma^2 v_s^2(\tau^2 + \sigma^2 v_s^2)}] \\
&\times[\mathrm{erf}[\frac{\tau^2(-r + R + v_s t) + R\sigma^2 v_s^2}{\sqrt{2}\sigma\tau v_s\sqrt{\tau^2 + \sigma^2 v_s^2}}] + \mathrm{erf}[\frac{\tau(r - v_s t)}{\sqrt{2}\sigma v_s\sqrt{\tau^2 + \sigma^2 v_s^2}}]] \\
&-2\sigma v_s\sqrt{\tau^2 + \sigma^2 v_s^2}[\exp[\frac{1}{2}R(-\frac{-2r + R + 2v_s t}{\sigma^2 v_s^2} - \frac{R}{\tau^2})] - 1]\} \qquad \text{(B.7)}
\end{aligned}$$

and

$$\begin{aligned}
J_2 \quad &= \int_0^R r' \exp[-\frac{r'^2}{2\tau^2} - \frac{(\frac{r+r'}{v_s} - t)^2}{2\sigma^2}]dr' \\
&= \frac{\sigma\tau^2 v_s}{2(\tau^2 + \sigma^2 v_s^2)^{3/2}} \exp[-\frac{(r + R - v_s t)^2}{2\sigma^2 v_s^2} - \frac{R^2}{2\tau^2}] \\
&\times\{\sqrt{2\pi}\tau(r - v_s t) \exp[\frac{(\tau^2(r + R - v_s t) + R\sigma^2 v_s^2)^2}{2\sigma^2\tau^2 v_s^2(\tau^2 + \sigma^2 v_s^2)}] \\
&\times[\mathrm{erf}[\frac{\tau(r - v_s t)}{\sqrt{2}\sigma v_s\sqrt{\tau^2 + \sigma^2 v_s^2}}] - \mathrm{erf}[\frac{\tau^2(r + R - v_s t) + R\sigma^2 v_s^2}{\sqrt{2}\sigma\tau v_s\sqrt{\tau^2 + \sigma^2 v_s^2}}]] \\
&+2\sigma v_s\sqrt{\tau^2 + \sigma^2 v_s^2}[\exp[\frac{R(2(r - v_s t) + \frac{R\sigma^2 v_s^2}{\tau^2} + R)}{2\sigma^2 v_s^2}] - 1]\}, \qquad \text{(B.8)}
\end{aligned}$$

respectively where $\mathrm{erf}(x)$ is the error function.Therefore, substituting the integrals J_1 and J_2 into Eq. B.5 gives

$$\begin{aligned}
p(r,t) \quad &= \frac{p_0\tau^2}{4r(\tau^2+\sigma^2 v_s^2)^{3/2}}\exp[-\frac{2R(r-v_s t)+2(r-v_s t)^2+R^2}{2\sigma^2 v_s^2}-\frac{R^2}{2\tau^2}] \\
&\times\{\sqrt{2\pi}\tau(r-v_s t)[\mathrm{erf}[\frac{\tau^2(-r+R+v_s t)+R\sigma^2 v_s^2}{\sqrt{2}\sigma\tau v_s\sqrt{\tau^2+\sigma^2 v_s^2}}] \\
&\times\exp[\frac{(r+R-v_s t)^2}{2\sigma^2 v_s^2}+\frac{\tau^2(r-v_s t)^2}{2\sigma^2 v_s^2(\tau^2+\sigma^2 v_s^2)}+\frac{R^2}{2\tau^2}] \\
&+\mathrm{erf}[\frac{\tau^2(r+R-v_s t)+R\sigma^2 v_s^2}{\sqrt{2}\sigma\tau v_s\sqrt{\tau^2+\sigma^2 v_s^2}}] \\
&\times\exp[\frac{\frac{(\tau^2(r+R-v_s t)+R\sigma^2 v_s^2)^2}{\tau^2(\tau^2+\sigma^2 v_s^2)}+(r-v_s t)^2}{2\sigma^2 v_s^2}]] \\
&-2\sigma v_s\sqrt{\tau^2+\sigma^2 v_s^2}\exp[\frac{(r-v_s t)^2}{2\sigma^2 v_s^2}][\exp[\frac{2R(r-v_s t)}{\sigma^2 v_s^2}]-1]\}. \qquad \text{(B.9)}
\end{aligned}$$

When the three cases based on the propagation time mentioned in the previous section are considered, the photoacoustic pressure wave takes its final form

$$\begin{aligned}
p(r,t) \quad &= \frac{p_0\tau^2}{4r(\tau^2+\sigma^2 v_s^2)^{3/2}}\exp[-\frac{2R(r-v_s t)+2(r-v_s t)^2+R^2}{2\sigma^2 v_s^2}-\frac{R^2}{2\tau^2}] \\
&\times\{\sqrt{2\pi}\tau(r-v_s t)[\mathrm{erf}[\frac{\tau^2(-r+R+v_s t)+R\sigma^2 v_s^2}{\sqrt{2}\sigma\tau v_s\sqrt{\tau^2+\sigma^2 v_s^2}}] \\
&\times\exp[\frac{(r+R-v_s t)^2}{2\sigma^2 v_s^2}+\frac{\tau^2(r-v_s t)^2}{2\sigma^2 v_s^2(\tau^2+\sigma^2 v_s^2)}+\frac{R^2}{2\tau^2}] \\
&+\mathrm{erf}[\frac{\tau^2(r+R-v_s t)+R\sigma^2 v_s^2}{\sqrt{2}\sigma\tau v_s\sqrt{\tau^2+\sigma^2 v_s^2}}] \\
&\times\exp[\frac{\frac{(\tau^2(r+R-v_s t)+R\sigma^2 v_s^2)^2}{\tau^2(\tau^2+\sigma^2 v_s^2)}+(r-v_s t)^2}{2\sigma^2 v_s^2}]] \\
&-2\sigma v_s\sqrt{\tau^2+\sigma^2 v_s^2}\exp[\frac{(r-v_s t)^2}{2\sigma^2 v_s^2}][\exp[\frac{2R(r-v_s t)}{\sigma^2 v_s^2}]-1]\} \\
&\times\theta(r-\mid R-v_s t\mid)\theta(-r+R+v_s t) \qquad \text{(B.10)}
\end{aligned}$$

for outside the spherical object. Hence, Eq. B.10 gives the photoacoustic pressure wave generated by a short laser pulse which has both Gaussian temporal and radial profiles.

For biomedical optics applications, we take realistic values of $v_s = 1480 m/s$, $\sigma = 6.5 ns$, and $R = 3mm$ [9, 18]. In Figure B.1, we observe the change of the normalized photoacoustic wave $\frac{p(r,t)}{p_0}$ as a function the normalized time $\frac{v_s t}{R}$ for $\frac{R}{\tau} = 1-10$ values using Eq. B.10. In Figure B.1, the photoacoustic wave has a different shape rather than a linear form when τ, beamwidth of the laser pulse, becomes comparable with the size of the spherical object, R. From Figs. 2 and 3, it is seen that the amplitude of the signal diminishes with increasing radial position.

In Figure B.1 using Eq. B.10, the change of the normalized pressure wave is observed with increasing pulse duration σ at $t = 5\mu s$ for various τ in the range of realistic pulse duration values. Figure B.1 shows that the photoacoustic wave is a decreasing function of the pulse duration because according to the following expression

$$E = P_{\text{peak}}\sigma, \tag{B.11}$$

the pulse duration is inversely proportional to peak power of the laser provided that the energy of the laser is constant where E and P_{peak} are energy and peak power of the laser, respectively. Hence, shorter pulse duration yields larger amplitude of photoacoustic wave by keeping in mind that depth resolution deteriorates.

Figure B.1 shows that as $\frac{R}{\tau}$ increases, the change of the normalized signal decreases slightly because the radial profile becomes very sharp and behaves like a Dirac delta function so that the laser parameters (pulse duration and beamwidth) begin to lose their effects on the signal.

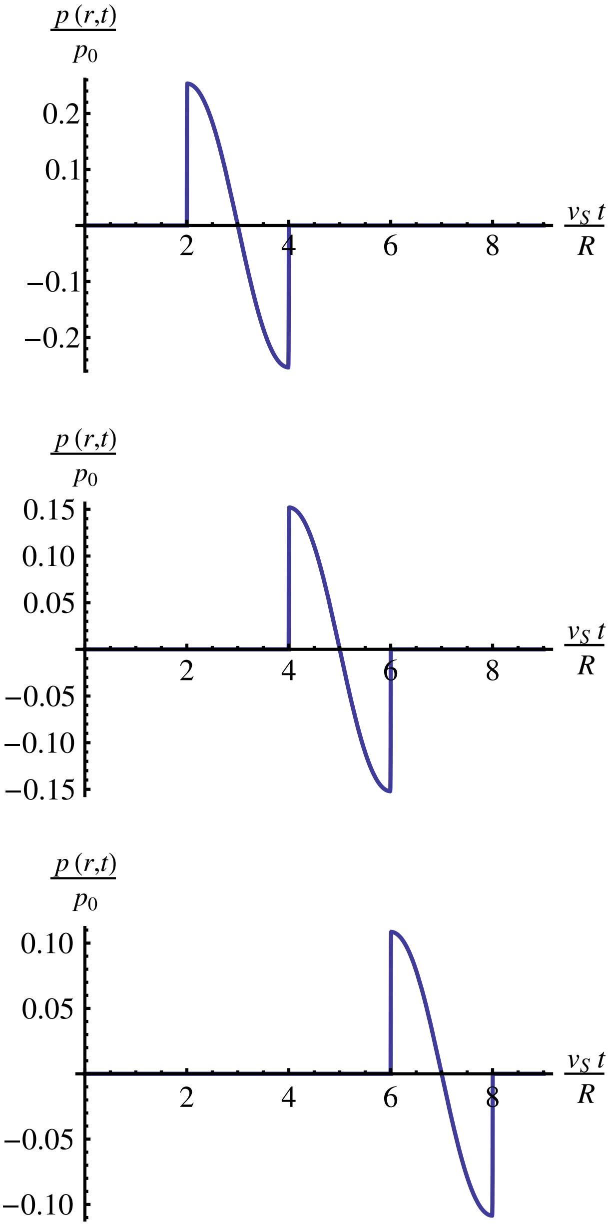

Figure B.1 Normalized photoacoustic pressure wave $\frac{p(r,t)}{p_0}$ vs. normalized time $\frac{v_s t}{R}$ for Gaussian temporal and rectangular radial profiles observed at different radial positions (a) $r = 3R$ (b) $r = 5R$ (c) $r = 7R$ where $\frac{\tau}{R} = 1$ [24].

REFERENCES

1. Leung, B. O., and K. C. Chou, “Review of super-resolution fluorescence microscopy for biology.,” *Applied spectroscopy*, Vol. 65, pp. 967–80, Sept. 2011.
2. Toomre, D., and J. Bewersdorf, “A new wave of cellular imaging.,” *Annual review of cell and developmental biology*, Vol. 26, pp. 285–314, Jan. 2010.
3. Hell, S. W., and J. Wichmann, “Breaking the diffraction resolution limit by stimulated emission: stimulated-emission-depletion fluorescence microscopy,” *Optics letters*, Vol. 19, no. 11, pp. 780–782, 1994.
4. Lidke, K. A., B. Rieger, T. M. Jovin, and R. Heintzmann, “Superresolution by localization of quantum dots using blinking statistics,” *Opt. Express*, Vol. 13, no. 18, pp. 7052–7062, 2005.
5. Betzig, E., G. H. Patterson, R. Sougrat, O. W. Lindwasser, S. Olenych, J. S. Bonifacino, M. W. Davidson, J. Lippincott-Schwartz, and H. F. Hess, “Imaging intracellular fluorescent proteins at nanometer resolution,” *Science*, Vol. 313, no. 5793, pp. 1642–1645, 2006.
6. Rust, M. J., M. Bates, and X. Zhuang, “Sub-diffraction-limit imaging by stochastic optical reconstruction microscopy (storm),” *Nature methods*, Vol. 3, no. 10, pp. 793–796, 2006.
7. Hess, S. T., T. P. Girirajan, and M. D. Mason, “Ultra-high resolution imaging by fluorescence photoactivation localization microscopy,” *Biophysical journal*, Vol. 91, no. 11, pp. 4258–4272, 2006.
8. Gustafsson, M. G., L. Shao, P. M. Carlton, C. Wang, I. N. Golubovskaya, W. Z. Cande, D. A. Agard, and J. W. Sedat, “Three-dimensional resolution doubling in wide-field fluorescence microscopy by structured illumination,” *Biophysical Journal*, Vol. 94, no. 12, pp. 4957–4970, 2008.
9. Wang, L. V., “Tutorial on photoacoustic microscopy and computed tomography,” *IEEE Journal of Selected Topics in Quantum Electronics*, Vol. 14, no. 1, pp. 171–179, 2008.
10. Wang, L. V., and S. Hu, “Photoacoustic tomography: in vivo imaging from organelles to organs,” *Science*, Vol. 335, no. 6075, pp. 1458–1462, 2012.
11. Maslov, K., H. F. Zhang, S. Hu, and L. V. Wang, “Optical-resolution photoacoustic microscopy for in vivo imaging of single capillaries,” *Opt. Lett.*, Vol. 33, pp. 929–931, May 2008.
12. Yuan, Y., S. Yang, and D. Xing, “Optical-resolution photoacoustic microscopy based on two-dimensional scanning galvanometer,” *Applied Physics Letters*, Vol. 100, no. 2, pp. 023702–023702–3, 2012.
13. Yao, J., and L. V. Wang, “Photoacoustic tomography: fundamentals, advances and prospects,” *Contrast media & molecular imaging*, Vol. 6, no. 5, pp. 332–345, 2011.
14. Bell, A. G. *Am.J.Sci*, Vol. 20, no. 305, 1880.
15. Rosencwaig, A., and A. Gersho, “Theory of the photoacoustic effect with solids,” *Journal of Applied Physics*, Vol. 47, p. 64, 1976.

16. Tam, A. C., "Applications of photoacoustic sensing techniques," *Reviews of Modern Physics*, Vol. 58, no. 2, p. 381, 1986.

17. Brewer, R., and C. Bruce, "Photoacoustic spectroscopy of NH_3 at the 9-μm and 10-μm $^{12}C^{16}O_2$ laser wavelengths," *Applied Optics*, Vol. 17, no. 23, pp. 3746–3749, 1978.

18. Wang, L. V., and H. Wu, *Biomedical Optics: Principles and Imaging*, Wiley Intersicence, 2007.

19. Ntziachristos, V., "Going deeper than microscopy with multi-spectral optoacoustic tomography (msot)," in *Asia Communications and Photonics Conference and Exhibition*, p. TuM1, Optical Society of America, 2009.

20. Dima, A., and V. Ntziachristos, "Non-invasive carotid imaging using optoacoustic tomography," *Opt. Express*, Vol. 20, pp. 25044–25057, Oct 2012.

21. Scruby, C. D., and L. E. Drain, *Laser Ultrasonics: Techniques and Applications*, Taylor and Francis, 1990.

22. Ntziachristos, V., J. Ripoll, L. V. Wang, and R. Weissleder, "Looking and listening to light: the evolution of whole-body photonic imaging," *Nature biotechnology*, Vol. 23, no. 3, pp. 313–320, 2005.

23. Morse, P. M., and H. Feshbach, *Methods of Theoretical Physics, Part I*, New York: McGraw-Hill, June 1953.

24. Erkol, H., E. Aytac-Kipergil, M. U. Arabul, and M. B. Unlu, "Analysis of laser parameters in the solution of photoacoustic wave equation," in *SPIE BiOS*, Vol. 8581, pp. 858136–858136–11, 2013.

25. Hoelen, C. G. A., and F. F. M. de Mul, "A new theoretical approach to photoacoustic signal generation," *J. Acoust. Soc. Am.*, Vol. 106, no. 2, pp. 695–706, 1999.

26. Cai, X., B. S. Paratala, S. Hu, B. Sitharaman, and L. V. Wang, "Multiscale photoacoustic microscopy of single-walled carbon nanotube-incorporated tissue engineering scaffolds," *Tissue Engineering Part C: Methods*, Vol. 18, no. 4, pp. 310–317, 2011.

27. Wang, L., K. Maslov, W. Xing, A. Garcia-Uribe, and L. V. Wang, "Video-rate functional photoacoustic microscopy at depths," *Journal of Biomedical Optics*, Vol. 106007, p. 1, 2012.

28. Okamoto, K., *Fundamentals of optical waveguides*, Elsevier, 2010.

29. Buck, J. A., "Fundamentals of optical fibers," *Fundamentals of Optical Fibers,*, Vol. 1, p. 352, April 2004.

30. Hariharan, P., *Basics of holography*, Cambridge University Press, 2002.

31. Paschotta, R., *Encyclopedia of Laser Physics and Technology*, Wiley-VCH, Berlin, 1 ed., 2008.

32. Bohren, C. F., and D. R. Huffman, *Absorption and Scattering of Light by Small Particles*, Wiley-Interscience, New York, 1983.

33. Hale, G. M., and M. R. Querry, "Optical constants of water in the 200-nm to 200-μm wavelength region," *Applied optics*, Vol. 12, no. 3, pp. 555–563, 1973.

34. Pope, R. M., E. S. Fry, *et al.*, "Absorption spectrum (380-700 nm) of pure water. ii. integrating cavity measurements," *Applied optics*, Vol. 36, no. 33, pp. 8710–8723, 1997.

35. Sogandares, F. M., and E. S. Fry, "Absorption spectrum (340–640 nm) of pure water. i. photothermal measurements," *Applied Optics*, Vol. 36, no. 33, pp. 8699–8709, 1997.

36. Kou, L., D. Labrie, and P. Chylek, "Refractive indices of water and ice in the 0.65-to 2.5-μm spectral range," *Applied Optics*, Vol. 32, no. 19, pp. 3531–3540, 1993.

37. Cope, M., *The development of a near infra red spectroscopy system and its application for non invasive monitoring of cerebral blood and tissue oxygenation in the newborn infants.* PhD thesis, University Collage London, 1991.

38. Cheong, W.-F., S. Prahl, and A. Welch, "A review of the optical properties of biological tissues," *Quantum Electronics, IEEE Journal of*, Vol. 26, no. 12, pp. 2166–2185, 1990.

39. Prahl, S., "Optical absorption of hemoglobin," 1999.

40. Conway, J. M., K. H. Norris, and C. Bodwell, "A new approach for the estimation of body composition: infrared interactance.," *The American journal of clinical nutrition*, Vol. 40, no. 6, pp. 1123–1130, 1984.

41. van Veen, R. L., H. Sterenborg, A. Pifferi, A. Torricelli, and R. Cubeddu, "Determination of vis-nir absorption coefficients of mammalian fat, with time-and spatially resolved diffuse reflectance and transmission spectroscopy," in *Biomedical Topical Meeting*, Optical Society of America, 2004.

42. Karabutov, A. A., E. V. Savateeva, N. B. Podymova, and A. Oraevsky, "Backward mode detection of laser-induced wide-band ultrasonic transients with optoacoustic transducer," *Journal of Applied Physics*, Vol. 87, no. 4, pp. 2003–2014, 2000.

43. Allen, T. J., S. Alam, E. Z. Zhang, J. G. Laufer, D. J. Richardson, and P. C. Beard, "Use of a pulsed fibre laser as an excitation source for photoacoustic tomography," *Proc. of SPIE*, Vol. 7899, pp. 78991V–78991V–6, Feb. 2011.

44. Sigrist, M. W., and F. K. Kneubühl, "Laser-generated stress waves in liquids," *J. Acoust. Soc. Am.*, Vol. 64, no. 6, pp. 1652–1663, 1978.

45. Lai, H. M., and K. Young, "Theory of the pulsed optoacoustic technique," *J. Acoust. Soc. Am.*, Vol. 72, no. 6, pp. 2000–2007, 1982.

46. Hoelen, C. G. A., F. F. M. de Mul, R. Pongers, and A. Dekker, "Three-dimensional photoacoustic imaging of blood vessels in tissue," *Opt. Lett.*, Vol. 23, pp. 648–650, Apr 1998.

47. Diebold, G. J., T. Sun, and M. I. Khan, "Photoacoustic monopole radiation in one, two, and three dimensions," *Phys. Rev. Lett.*, Vol. 67, pp. 3384–3387, Dec 1991.

48. Inkov, V. N., A. A. Karabutov, and I. M. Pelivanov, "A theoretical model of the linear thermo-optical response of an absorbing particle immersed in a liquid," *Laser Physics*, Vol. 11, pp. 1283–1291, May 2001.

49. Kozhushko, V., T. Khokhlova, A. Zharinov, I. Pelivanov, V. Solomatin, and A. Karabutov, "Focused array transducer for two-dimensional optoacoustic tomography," *J. Acoust. Soc. Am.*, Vol. 116, pp. 1498–1506, Sep 2004.

50. Diebold, G. J., and J. Westervelt, “The photoacouctic effect generated by a spherical droplet in a fluid,” *J. Acoust. Soc. Am.*, Vol. 84, pp. 2245–2251, Dec 1988.

51. Maslov, K., G. Stoica, and L. V. Wang, “In vivo dark-field reflection-mode photoacoustic microscopy,” *Opt. Lett.*, Vol. 30, pp. 625–627, Mar 2005.

52. Maslov, K., H. F. Zhang, and L. V. Wang, “Effects of wavelength-dependent fluence attenuation on the noninvasive photoacoustic imaging of hemoglobin oxygen saturation in subcutaneous vasculature in vivo,” *Inverse Problems*, Vol. 23, pp. S113–S122, Dec. 2007.

53. Zhang, H. F., K. Maslov, and L. V. Wang, “In vivo imaging of subcutaneous structures using functional photoacoustic microscopy.,” *Nature protocols*, Vol. 2, pp. 797–804, Jan. 2007.

54. Zhang, E., J. Laufer, and P. Beard, “Backward-mode multiwavelength photoacoustic scanner using a planar fabry-perot polymer film ultrasound sensor for high-resolution three-dimensional imaging of biological tissues,” *Appl. Opt.*, Vol. 47, pp. 561–577, Feb 2008.

55. Jose, J., S. Manohar, R. G. M. Kolkman, W. Steenbergen, and T. G. van Leeuwen, “Imaging of tumor vasculature using Twente photoacoustic systems.,” *Journal of biophotonics*, Vol. 2, pp. 701–17, Dec. 2009.

56. Shi, W., S. Kerr, I. Utkin, J. Ranasinghesagara, L. Pan, Y. Godwal, R. J. Zemp, and R. Fedosejevs, “Optical resolution photoacoustic microscopy using novel high-repetition-rate passively q-switched microchip and fiber lasers.,” *Journal of Biomedical Optics*, Vol. 15, no. 5, p. 056017, 2010.

57. Shi, W., P. Hajireza, P. Shao, A. Forbrich, and R. J. Zemp, “In vivo near-realtime volumetric optical-resolution photoacoustic microscopy using a high-repetition-rate nanosecond fiber-laser,” *Opt. Express*, Vol. 19, pp. 17143–17150, Aug 2011.

58. Liu, M., and T. Buma, “Wavelength agile photoacoustic microscopy with a pulsed supercontinuum source,” in *Ultrasonics Symposium (IUS), 2010 IEEE*, pp. 382–385, 2010.

59. Yeh, C., S. Hu, K. Maslov, and L. V. Wang, “Photoacoustic microscopy of blood pulse wave,” *Journal of Biomedical Optics*, Vol. 17, no. 7, pp. 070504–1–070504–3, 2012.

60. Yeh, C., S. Hu, K. Maslov, and L. V. Wang, “Blood pulse wave velocity measured by photoacoustic microscopy,” in *SPIE BiOS*, Vol. 8581, pp. 85812C–85812C–6, 2013.

61. Maslov, K., S. Hu, and L. V. Wang, “Second generation optical-resolution photoacoustic microscopy,” in *SPIE BiOS*, pp. 789933–789933, International Society for Optics and Photonics, 2011.

62. Zeng, L., G. Liu, D. Yang, and X. Ji, “Portable optical-resolution photoacoustic microscopy with a pulsed laser diode excitation,” *Applied Physics Letters*, Vol. 102, no. 5, pp. 053704–053704, 2013.

63. Haus, H., “Mode-locking of lasers,” *Selected Topics in Quantum Electronics, IEEE Journal of*, Vol. 6, no. 6, pp. 1173–1185, 2000.

64. Özgören, K., B. Öktem, S. Yilmaz, F. Ömer Ilday, and K. Eken, “83 w, 3.1 MHz, square-shaped, 1 ns-pulsed all-fiber-integrated laser for micromachining,” *Opt. Express*, Vol. 19, pp. 17647–17652, Aug 2011.

65. Kumar, V., A. George, W. Reeves, J. Knight, P. Russell, F. Omenetto, and A. Taylor, “Extruded soft glass photonic crystal fiber for ultrabroad supercontinuum generation,” *Optics Express*, Vol. 10, no. 25, pp. 1520–1525, 2002.

66. Dudley, J. M., G. Genty, and S. Coen, “Supercontinuum generation in photonic crystal fiber,” *Rev. Mod. Phys.*, Vol. 78, pp. 1135–1184, Oct 2006.

67. Alfano, R. R., and S. L. Shapiro, “Observation of self-phase modulation and small-scale filaments in crystals and glasses,” *Phys. Rev. Lett.*, Vol. 24, pp. 592–594, Mar 1970.

68. Harbold, J. M., F. O. Ilday, F. W. Wise, T. A. Birks, W. J. Wadsworth, and Z. Chen, “Long-wavelength continuum generation about the second dispersion zero of a tapered fiber,” *Opt. Lett.*, Vol. 27, pp. 1558–1560, Sep 2002.

69. Grosso, V. A. D., and C. W. Mader, “Speed of sound in pure water,” *The Journal of the Acoustical Society of America*, Vol. 52, no. 5B, pp. 1442–1446, 1972.

70. Hoskins, P. R., K. Martin, and A. Thrush, *Diagnostic ultrasound: physics and equipment*, Cambridge University Press, 2010.

71. Wang, L. V., “Ultrasound-mediated biophotonic imaging: A review of acousto-optical tomography and photo-acoustic tomography,” *Disease Markers*, Vol. 19, no. 2, pp. 123–138, 2004.